

# 1    **Structure of the crust and upper mantle beneath Bass Strait, southeast** 2    **Australia, from teleseismic body wave tomography**

3    M. Bello<sup>\*1,2</sup>, N. Rawlinson<sup>3</sup>, D. G. Cornwell<sup>1</sup>, E. Crowder<sup>1</sup>, M. Salmon<sup>4</sup> & A. M. Reading<sup>5</sup>

4    <sup>1</sup>School of Geosciences, University of Aberdeen, Aberdeen UK

5    <sup>2</sup>Department of Physics, Abubakar Tafawa Balewa University, Bauchi, Nigeria

6    <sup>3</sup>Department of Earth Sciences – Bullard Labs, University of Cambridge, Cambridge, UK

7    <sup>4</sup>Research School of Earth Sciences, The Australian National University, Canberra, Australia

8    <sup>5</sup>School of Natural Sciences (Physics), University of Tasmania, Hobart, TAS 7001, Australia

9

10        We present new constraints on the lithospheric velocity structure of Bass Strait and the adjoining  
11        landmasses of mainland Australia and Tasmania in order to better constrain their geological and  
12        tectonic relationship. This is achieved by performing teleseismic tomography using data from fifteen  
13        deployments of WOMBAT and BASS transportable arrays, which span southeastern Australia. The  
14        starting model for the teleseismic tomography includes crustal velocity structure constrained by  
15        surface waves extracted from ambient seismic noise data and a Moho surface and broad-scale  
16        variations in 3-D upper mantle velocity structure from the Australian seismological reference Earth  
17        model (AuSREM). As a consequence, we produce a model with a high level of detail in both the  
18        crust and upper mantle. Our new results strengthen the argument for a low velocity upper mantle  
19        anomaly that extends down to ~150 km depth directly beneath the Newer Volcanics Province in  
20        Victoria, which is likely related to recent intra-plate volcanism. Beneath Bass Strait, which is thought  
21        to host the entrained VanDieland microcontinent, upper mantle velocities are low relative to those  
22        typically found beneath Precambrian continental crust; it is possible that failed rifting in Bass Strait  
23        during the Cretaceous, opening of the Tasman Sea, extension of VanDieland during Rodinian break-  
24        up and recent plume activity in the past 5 Ma may have altered the seismic character of this region.  
25        The data nevertheless suggest: (1) the velocity structure of the VanDieland microcontinent lacks  
26        continuity within its lithosphere; (2) the Moyston Fault defines an area of strong velocity transition at  
27        the boundary between the Cambrian Delamerian Orogen and the Cambrian-Carboniferous Lachlan  
28        Orogen; and (3) there is a rapid decrease in mantle velocity inboard of the east coast of Australia,  
29        which is consistent with substantial thinning of the lithosphere towards the passive margin.

30

31    **KEY WORDS:** teleseismic tomography, body waves, surface waves, upper mantle, Bass Strait, southeast Australia

32

## 33    **1. Introduction**

34

35 As a result of numerous studies carried out in southeastern Australia (Boger and Miller, 2004;  
36 Cawood, 2005; Cayley, 2011; White et al., 2013; Moresi et al., 2014; Pilia et al., 2015a, 2015b;  
37 Moore et al., 2015, 2016 - for earlier studies, see references in these publications), knowledge of the  
38 geological and tectonic relationship between mainland Australia and Tasmania, which are separated  
39 by Bass Strait, has markedly improved over the past few decades (see Fig. 1 for geological map).  
40 However, very little can be inferred about the lower crust and mantle lithosphere from these studies,  
41 and consequently, a more complete picture of the region is yet to emerge.

42  
43 The main difficulties in linking Tasmania and mainland Australia are the presence of Bass Strait,  
44 which separates the two land masses, the presence of three thick Cretaceous to recent sedimentary  
45 basins (Bass, Gippsland and Otway) and the widespread occurrence of recent intrusive and  
46 extrusive volcanism, which have largely prevented direct observation of the underlying basement  
47 rocks. Although gravity and magnetic data can provide useful insight into basement structures  
48 (Cayley et al., 2011; Moore et al., 2015, 2016), the thickness of the failed-rift sedimentary basins  
49 that formed during Australia-Antarctica breakup is a major obstacle for understanding the  
50 Proterozoic-Palaeozoic connection between the lithosphere of Tasmania and mainland Australia. To  
51 date, most models that attempt to connect Victoria and Tasmania either rely on the interpolation of  
52 information between outcrops in both states, with some additional constraints provided by potential  
53 field data (e.g. Leaman et al., 1994; Morse et al., 2009), geochemical investigations and seismic  
54 reflection profiling (e.g. O'Sullivan et al., 2000; Drummond et al., 2000). One hypothesis that has  
55 recently gained significant traction is that a fragment of Precambrian continental lithosphere, set  
56 adrift by the break-up of the supercontinent Rodinia, became entrained in the convergent  
57 accretionary system responsible for the formation of the Lachlan Orogen, and now underlies both  
58 western Tasmania and southern Victoria (Cayley et al., 2002; Direen and Crawford, 2003; Glen,  
59 2005; Cayley et al., 2011; Moresi et al., 2014; Moore et al., 2015, 2016). Ambient noise  
60 tomography has also been employed to image crustal structure beneath Bass Strait, with initial  
61 results pointing to the possible presence of a Precambrian continental fragment (Pilia et al., 2015a,  
62 2015b). In other studies that are based on stratigraphic and geochemical considerations, Black et al.  
63 (2004) found evidence for the presence of Precambrian lithosphere underlying Tasmania and King  
64 Island, and Meffre et al. (2004) concluded that the Neoproterozoic mafic volcanics and intrusive



65 sequences of eastern King Island have many geochemical and stratigraphic characteristics that  
66 indicate 579 Ma rifting associated with an extensive volcanic passive margin. All these studies focus  
67 mainly on the crustal portion of the lithosphere; as such, the inclusion of data capable of  
68 constraining the mantle lithosphere has the potential to shed new light on the structure and tectonic  
69 evolution of Bass Strait.

70

71 In this paper, we apply teleseismic tomography to a dataset recorded by the high density WOMBAT  
72 and BASS transportable seismic arrays, which comprise of over 620 stations, deployed during the  
73 course of 15 separate array movements. These datasets are combined for the first time to constrain  
74 3-D velocity perturbations in the upper mantle beneath Bass Strait. Teleseismic tomography utilises  
75 relative arrival time residuals from distant earthquake sources, recorded across an array of seismic  
76 stations, to image the seismic structure of the upper mantle beneath the array. A key assumption is  
77 that relative arrival time residuals across the receiver array are largely unaffected by lateral  
78 variations in the structure outside a local model volume defined beneath the array. Typically, shallow  
79 structure to a depth approximately equal to the station spacing (Rawlinson et al., 2010) is not  
80 constrained due to the near-vertical trajectories of impinging teleseismic rays. Here, we address this  
81 limitation by incorporating an ambient noise crustal model in our starting model. Another  
82 improvement, compared to traditional schemes, is the incorporation of an explicit Moho surface and  
83 large-scale mantle velocity variation in the starting model, which are sourced from the AuSREM  
84 model of the Australian continent (Kennett and Salmon, 2013).

85

86 Teleseismic body wave tomography has been frequently used in various parts of the world (Aki et  
87 al., 1977; Oncescu et al., 1984; Humphreys and Clayton, 1990; Achauer, 1994; Steck et al., 1998;  
88 Lippitsch et al., 2003; Rawlinson et al., 2006) but has never been applied to study the upper mantle  
89 beneath Bass Strait. However, teleseismic tomography studies have been carried out in northern  
90 Tasmania (Rawlinson et al., 2006) and southeastern mainland Australia (Graeber et al., 2002;  
91 Rawlinson and Kennet, 2008; Rawlinson et al., 2011; Rawlinson and Fishwick, 2012; Rawlinson et  
92 al., 2015; Rawlinson et al., 2016), but they have only been able to yield limited insight into the  
93 relationship between the two landmasses. The inclusion of the BASS dataset, which spans Bass  
94 Strait, together with adjacent data from the mainland and Tasmania, provides a unique opportunity

95 to image this region in detail using seismic techniques.

96

## 97 **2. Data and Method**

### 98 **2.1 Teleseismic data**

99 The teleseismic data for this study come from the WOMBAT transportable seismic array  
100 deployments between 1998 and 2012 and the recent BASS array, which was deployed from 2011 to  
101 2013 (Fig. 2). Each WOMBAT deployment involves between 20 to 70 stations deployed as a single  
102 array, which after 6-12 months is transported to an adjacent location in order to achieve a high  
103 density coverage over a large region. The average spacing between WOMBAT stations varies from  
104 15 km in Tasmania to 50 km on the mainland. The seismometers used for this array are either 1 Hz  
105 vertical component L4Cs (up until 2006), or 3-component 1Hz Lennartz LE-3Dlites. A number of  
106 arrays (e.g. TIGGER and SEAL2) also incorporate several broadband seismometers (Guralp 40T or  
107 3ESP).

108 In the case of the BASS array, the dataset consists of approximately 23 months (May 2011 to April  
109 2013) of passive seismic data recorded by an array of 24 three-component broadband instruments  
110 covering southern Victoria, several islands in Bass Strait (Flinders, King and Deal islands) and  
111 northern Tasmania (Fig. 2). The instruments consist of 23 Guralp 40T and one Guralp 3ESP  
112 broadband sensors. The 40T instrument has a flat response from 50Hz to 30s period and the 3ESP  
113 has a flat response from 50Hz to 60s period. The instruments are connected to Earth Data PR6-24  
114 portable field recorders.

115 The teleseismic dataset is characterised by dominant source regions to the north and east and a  
116 much lower concentration of sources to the west and south of the study area. A total of 53,957 P-  
117 wave relative arrival time residuals from 1558 events are used in the teleseismic tomography; since  
118 we are using a transportable array (combined total of 624 receivers from 15 sequential  
119 deployments), each event is only recorded by the sub-array which was operating at the time that it  
120 took place. Teleseismic events with an angular distance  $>27^\circ$  (from the centre of each array) and  $M_w$   
121  $\geq 5.5$  are considered. Figure 3 shows a plot of the locations of all teleseismic events used in this  
122 study.

## 123    **2.2 Arrival time residual estimation and inversion**

124    The coherence of teleseismic arrivals across dense seismic arrays allows the relative onset times of  
125    various global phases to be estimated with high accuracy. In this study, the adaptive stacking  
126    scheme of Rawlinson and Kennett (2004) is used to extract residuals from the BASS array.  
127    Residuals from the Tasmanian and mainland arrays were extracted using exactly the same procedure  
128    described in previous studies (Rawlinson and Urvoy, 2006; Rawlinson et al., 2016). Adaptive  
129    stacking exploits the similarity between waveforms to provide a rapid, accurate and robust  
130    procedure for estimating the residual patterns across a network of seismic stations. Following any  
131    pre-processing of the data (in our case, unifying instrument responses and band pass filtering  
132    between 0.3-5.0 Hz), the first step of the scheme involves approximate alignment of all filtered  
133    traces according to predictions from a propagation model (ak135), which are then stacked to form a  
134    reference trace. Iterative improvement of the alignment, by comparison of the reference trace with  
135    each station trace, leads to a direct estimate of the residuals relative to the 1-D propagation model.  
136    This technique has proven to be fast and works well in the presence of noisy data and some  
137    waveform distortion (Rawlinson and Kennett, 2004). Figure 5 shows an example of adaptive stack-  
138    ing applied to traces from the BASS array experiment.

139    The arrival time residuals are mapped as 3D perturbations in P-wave velocity with respect to a  
140    reference model using teleseismic tomography. The teleseismic tomography method assumes that  
141    relative arrival time residuals across the array are largely unaffected by lateral structural variations  
142    from outside the local 3-D model volume beneath the array. The software package FMTOMO was  
143    used to perform the teleseismic tomography; FMTOMO uses the Fast Marching Method (FMM)  
144    (Sethian, 1996; Sethian and Popovici, 1999; Rawlinson and Sambridge, 2004a, 2004b; de Kool et  
145    al., 2006) for the forward prediction step and a subspace inversion scheme to adjust model  
146    parameters in order to match observed and predicted traveltimes subject to damping and  
147    smoothing regularisation (Kennett et al., 1988). The method is iterative non-linear in that the  
148    inversion step assumes local linearity, but repeated application of FMTOMO and subspace  
149    inversion allows the non-linear relationship between velocity and traveltimes perturbations to be  
150    reconciled (see Rawlinson and Urvoy, 2006, and Rawlinson et al., 2016 for more information on  
151    FMTOMO).

## 152    **2.3 3-D Starting model**

### 153    **2.3.1 Crustal model**

154    In order to mitigate a recognised weakness of teleseismic tomography- its inability to accurately  
155    constrain shallow structure to a depth roughly equal to the station spacing (e.g. Rawlinson et al.,  
156    2010) - a high resolution crustal model derived from ambient noise data that properly accounts for  
157    the crustal contribution to the measured arrival time residuals was included in the starting model for  
158    the inversion of WOMBAT and BASS teleseismic arrival time residuals (see section S1 of the sup-  
159    porting information). As an alternative to the AuSREM crustal velocity model, the crustal model de-  
160    rived from WOMBAT ambient seismic noise data contains well constrained features as small as 30–  
161    50 km horizontally and 2–5 km vertically. The robustness of this model is evident from the features  
162    recovered (Fig. 4), which share a strong association with the surface geology and constraints pro-  
163    vided by potential field data in this region. As such, we believe that it is the better model to use for  
164    crustal corrections of the teleseismic traveltime residuals

### 165    **2.3.2 Upper mantle model**

166    The AuSREM Moho model (Kennett et al., 2013) and broad scale mantle structure (Figs. 4c and 7  
167    respectively) were also included in the starting model. It is well known that relative arrival time  
168    residuals computed for adjacent arrays operating at different times are not directly comparable due  
169    to the average velocity structures beneath them likely being different (e.g. Rawlinson et al., 2016).  
170    Hence, unless we incorporate a robust 3-D reference model with a scale length less or equal to the  
171    aperture of the smallest seismic array that is used, or have a backbone array of stations that record  
172    throughout the durations of the transportable array experiment, then the solution model is likely to  
173    contain artifacts, including the loss of long-wavelength structure. In our case, the AuSREM mantle  
174    velocity model is sufficiently robust to allow the linking of the different WOMBAT and BASS rela-  
175    tive arrival time residual datasets in a joint inversion.

176    Seismic data exploited by AuSREM comes from over 12,000 km of deep crustal reflection profiles,  
177    a number of major refraction experiments, and many different passive seismic deployments (Kennett  
178    et al., 2013, Salmon et al., 2013). Due to moderate coverage of reflection data in this region and

179 constraints from receiver functions, the broadscale variations in AuSREM Moho geometry are likely  
180 to be reasonably robust. However, this is not true for crustal P-wave velocity, which is only con-  
181 strained by a few 2-D refraction experiments in the model region (Salmon et al., 2013); hence our  
182 use of an ambient noise crustal model in the 3-D starting model.

## 183    **2.4 Conversion of S to P velocity**

184 One limitation of the ambient noise model used for crustal correction is that it defines S-wave veloc-  
185 ities, whereas the teleseismic arrival time residuals come from global P-phases. We cannot use S-  
186 phases in this study because the majority of WOMBAT stations are short period (~1 Hz corner fre-  
187 quency), which makes teleseismic S-arrivals difficult to detect in comparison to P. In order to con-  
188 vert from S-wave velocity to P-wave velocity, we apply the same approach as Rawlinson et al.  
189 (2016), who use the AuSREM crustal  $V_p/V_s$  model (Salmon et al., 2013); although it features lower  
190 lateral resolution compared to our new lithospheric model, the peak  $V_p/V_s$  perturbations are only  
191 around ~3% which are unlikely to be a factor in the correction of P-wave arrival time residuals for  
192 crustal structure.

## 193    **3. Results**

194  
195 We represent the seismic structure of the southeast Australian lithosphere using a two-layer model  
196 consisting of a crust and upper mantle separated by a Moho surface. Compared to previous teleseis-  
197 mic studies that exploit WOMBAT data to image the lithosphere beneath southeast Australia (Grae-  
198 ber et al., 2002; Rawlinson et al., 2006, 2011; Clifford et al., 2008; Rawlinson and Kennett, 2008;  
199 Fishwick and Rawlinson, 2012; Rawlinson et al., 2015, 2016), the work presented here uses a geo-  
200 graphically more extensive dataset that also covers Bass Strait and northern Tasmania. However, the  
201 broad-scale variations in wave speed in regions that overlap with previous studies are in general  
202 agreement; this is a reassuring sign when sequential studies are performed in the same region using  
203 increasingly large datasets and/or different tomographic imaging schemes (Fishwick and Rawlinson,  
204 2012).

205 The inversion result was obtained by using six iterations of FMTOMO, with a starting model de-  
206 fined by 459,000 velocity nodes and 7650 interface nodes. The data misfit component of the objec-

207 tive function is based on the difference between observed residuals and model residuals. In the latter  
208 case, these residuals are computed by taking the difference between predictions through the recov-  
209 ered model (with receivers set at the correct elevation) at each iteration and ak135 reference model  
210 predictions (with receivers set to zero elevation). Therefore, contributions to the predicted residual  
211 from crustal velocity, Moho geometry and long wavelength mantle structure is accounted for, as is  
212 the fact that adaptive stacking residuals were calculated using move-out corrections under the as-  
213 sumption that all receivers were at the same elevation. It is important to note, therefore, that the  
214 starting model for the inversion, which contains lateral structure in the crust, mantle and Moho, is  
215 not the same as the laterally invariant model used to compute the reference arrival times. In order to  
216 produce a model that does not greatly deviate from the starting model and contains no unnecessary  
217 features, while at the same time having an acceptable fit to the data, damping and smoothing values  
218 are chosen using the approach of Rawlinson et al. (2006) which is based on a three step procedure  
219 using trade-off curves between data variance and model variance, and data variance and model  
220 roughness (Fig. 6). This involves running a series of inversions with different levels of damping and  
221 smoothing in order to identify the model with minimum perturbation and roughness that still satis-  
222 fies the data to an acceptable level. If we assume that the point of maximum curvature on the trade-  
223 off curve provides the optimum compromise, then both the damping and smoothing values are ~200  
224 in our case (Fig. 6). However, it is well known that this approach is ad-hoc, and following extensive  
225 testing, we ultimately prefer to use the same damping and smoothing (75 in both cases) as Rawlin-  
226 son et al. (2016) which produces a slightly underdamped and undersmoothed version of the opti-  
227 mum model (according to the trade-off curves). We believe that this model reveals features that are  
228 more consistent with crustal structure (from ambient noise tomography) and broadscale surface ge-  
229 ology. However, the differences between the two models are not large, with our preferred model ex-  
230 hibiting a very similar pattern of anomalies, albeit with slightly larger amplitude (see Supplemen-  
231 tary Figs. S1-S3 for models produced using various damping and smoothing values, including the  
232 “optimum” model according to the trade-off curves). The final solution model, based on damping  
233 and smoothing values of 75, resulted in a variance reduction in the traveltime residual misfit of 73%  
234 relative to the starting 3-D model (and 78% relative to ak135). Below, we present the results of a  
235 synthetic recovery test and the solution model for mantle P-wave velocities.

### 236 3.1 Synthetic test

237 Because of solution non-uniqueness in seismic tomography problems a single data-satisfying model  
238 may contain features that are not required by the data. Therefore, before interpreting our solution  
239 model, the robustness of the data constraints is first investigated using a synthetic checkerboard test  
240 (Glahn and Granet, 1993; Ritsema et al., 1998; Day et al., 2001; Rawlinson and Sambridge, 2003;  
241 Rawlinson and Kenneth, 2008). This test involves using the identical sources, receivers and phase  
242 types from the observational dataset to predict the arrival time-residuals for a synthetic structure  
243 comprising an alternating 3D pattern of fast and slow velocities, separated by a narrow region of  
244 zero perturbation (Fig. 8a and c). Here, we are only testing the resolving power of the teleseismic  
245 dataset, because the crustal velocities are derived from ambient noise tomography alone and have no  
246 dependence on the mantle velocities or teleseismic data. Hence, velocity anomalies are only  
247 imposed on upper mantle structure, and both crustal velocity variations and the AuSREM Moho are  
248 held fixed.

249 Prior to running an inversion for recovery of the synthetic checkerboard, Gaussian noise with a  
250 standard deviation of 59 ms was added to the synthetic dataset. This is equal to the standard  
251 deviation of the noise estimated by the adaptive stacking procedure used to extract the relative  
252 arrival time residuals. The predicted data are then inverted using the same tomographic procedure  
253 that is applied to the observations. Following the inversion, the difference between the input and  
254 output models can be used as a measure of how well structure can be recovered (Fig. 8b and d). This  
255 test is often favoured in seismic tomography (e.g. Graeber and Asch, 1999; Rawlinson et al., 2011)  
256 because a continuous pattern makes interpretation relatively straight forward; however, it cannot be  
257 regarded as a comprehensive test of solution robustness (Lévêque et al., 1993; Rawlinson and  
258 Spakman, 2016).

259 The east – west cross-sections through the checkerboard inversion model (Fig. 9(A-A')) generally  
260 exhibit good recovery, although there is some smearing of structure towards the edge of the array  
261 caused by a predominance of paths with similar orientations. The north – south cross-sections (Fig.  
262 9(B-B')) also recover some of the checkerboard pattern, although smearing is clearly evident beyond  
263 the horizontal bounds of the array. Similarly, the centre of Bass Strait is poorly recovered at shallow

264 depth, which can be attributed to an absence of receivers (such as ocean bottom seismometers) in  
265 the marine environment. The minimum scale length of structure that can be recovered by  
266 teleseismic tomography is typically equal to the station spacing (Rawlinson et al., 2015), which in  
267 this case is around 50 km, similar to the mainland station spacing. In summary, the upper mantle  
268 structure appears to be well constrained by the path coverage, although resolution tends to decrease  
269 beyond the horizontal bounds of the seismic array (see Supplementary Figs. S4 for additional  
270 checkerboard recovery tests).

### 271 **3.2 WOMBAT-BASS model**

272 The model recovered from inversion of WOMBAT and BASS teleseismic datasets is shown in  
273 Figures 10, 11 and 12 (note that the grey mask denotes less resolved areas as determined by  
274 inspection of checkerboard test results), and reveals a number of significant structural features. The  
275 horizontal slice at 75 km depth (Fig. 10) shows an E-W (latitude  $37.2^{\circ}$  S) trending low velocity  
276 anomaly in the upper mantle in southern Victoria (see dashed rectangle SV), which lies to the north  
277 of a narrow high velocity anomaly located along the SE Victorian coast. Bass Strait appears as a  
278 relatively low velocity zone (noting that it is not well resolved in the centre at this depth) while  
279 upper mantle velocities in northern Tasmania vary from fast to slow to fast from west to east (see  
280 dashed rectangle NT in Fig. 10). North of the line A-A' in Figure 10, the model is largely consistent  
281 with the body wave tomography model of Rawlinson et al. (2016), which uses the same mainland  
282 arrival time residual dataset from WOMBAT. At greater depths beneath the southern region of the  
283 model, the pattern of velocity anomalies becomes less coherent, but the lower velocities beneath  
284 southern Victoria and Bass Strait and the higher velocities to the north extend to well over 100 km  
285 depth (B-B' in Fig. 11). In general, the pattern of residuals in the crust and Moho variations do not  
286 appear to share an overall anti-correlation with uppermost mantle anomalies, which at least suggests  
287 that crustal structure is not dictating upper mantle structure.

288 In order to reinforce the importance of a 3-D starting model in improving the recovery of mantle  
289 structure, a comparative test was carried out. Here, the inversion of the data was carried out using a  
290 purely 1-D starting model (ak135) in the crust and upper mantle, and a flat Moho consistent with  
291 ak135. The recovered model in Figure 13 shows clear similarities and differences with the solution



292 produced using a 3-D starting model (Fig. 12). The lack of longer wavelength structures in Figure  
293 13, particularly evident in the cross-sections, would make interpretation more challenging if this  
294 model was considered in isolation. Furthermore, while there is general agreement on the shorter  
295 wavelength structures, there are differences evident, particularly at shallow mantle depths. Of  
296 particular relevance to this study is the presence of high velocity anomalies appearing to connect  
297 Tasmania and Victoria across Bass Strait in the 75 km and 120 km depth slices of Figure 13. This  
298 may lead one to conclude that the two share a structural connection in the mantle lithosphere, but as  
299 Figure 12 demonstrates, these anomalies are more likely to be artifacts caused by the vertical  
300 smearing of unresolved crustal structure.

## 301 **4. Discussion**

302 The inversion of the WOMBAT-BASS dataset has produced a high resolution lithospheric velocity  
303 model of Bass Strait and adjoining southeast mainland Australia and Tasmania. Many intriguing  
304 features are observed in our P-wave velocity model that could pertain to tectonic processes that  
305 affected the study area. Several velocity anomalies imaged in our study are present in previously  
306 determined models of northern Tasmania and southern Victoria. These include the high velocities  
307 found in the upper mantle beneath the Rocky Cape Block of north-west Tasmania (Rawlinson and  
308 Urvoy, 2006; Rawlinson and Kennett, 2008) and regions of low mantle velocity beneath the Tamar  
309 Fracture System (TFS) and Newer Volcanics Province (NVP) (Rawlinson and Fishwick, 2012;  
310 Rawlinson et al., 2015; Rawlinson et al., 2016). Further north, higher velocities associated with  
311 cratonic regions and lower velocities near the eastern seaboard, which are likely due to lithospheric  
312 thinning towards the passive margin, can be observed (Rawlinson et al., 2016). A recent study that  
313 also show consistency with our results in terms of lower velocities underneath the Lachlan Fold Belt  
314 and Bass Strait is that of Sun et al. 2016. In their study, they apply 3-D  $P_n$  travel time tomography to  
315 improve structural constraints on the uppermost mantle across the Australian continent. They find  
316 some of the lowest velocities beneath the southern Lachlan Fold Belt, the Newer Volcanics province  
317 and Bass Strait, which largely agrees with our teleseismic body wave tomography model, and  
318 supports the idea that recent intraplate volcanism, coupled with lithospheric thinning associated with  
319 failed rifting, have strongly influenced the seismic structure of the lithosphere in this region.

320 Our new tomographic model exhibits a distinct north dipping low velocity anomaly that extends  
321 from just below the crust to ~150 km depth in the upper mantle directly beneath the NVP (see Fig.  
322 12 cross-section A-A'). Previously, Davies et al. (2015) identify the world's longest continental hot-  
323 spot track (over 2000 km total length), which begins in north Queensland, and extends southward,  
324 possibly as far as NW Tasmania. Their study suggests that the plume source of the hotspot track  
325 passed by the eastern edge of the NVP shortly before volcanism initiated nearly 5 Ma. In another  
326 study, Rawlinson et al. 2017 suggest that an interaction between this passing plume and pre-existing  
327 Edge Driven Convection (EDC) (King and Anderson, 1998) and Shear Driven Upwelling (SDU)  
328 (King and Ritsema, 2000) (caused by a huge central cavity in the lithosphere, which corresponds to  
329 the central low velocity zone north of the NVP in our model) was responsible for the NVP volcan-  
330 ism. A more recent study by Wei et al. 2008 using 3-D  $S_n$  traveltimes tomography finds strong  
331 heterogeneities in S wave speed in the upper mantle across the entire Australian continent. They also  
332 include Pn data to determine the uppermost mantle Vp/Vs ratio across the whole continent. Their  
333 study finds distinctive localised low velocity anomalies beneath the eastern margin of Australia  
334 which they interpret as evidence of mantle plume remnants. Our model shows a low velocity zone  
335 beneath Bass Strait (Fig. 12 cross-section C-C'), but below 200 km depth these lower velocities dis-  
336 appear entirely. A recent study has suggested that the plume was waning as Australia gradually  
337 moved north (Jones and Verdel, 2015), so it is possible that there is no longer any clear evidence for  
338 it at greater depth. Nonetheless, it may have contributed to the lower velocities observed beneath  
339 Bass Strait.

340

341 Our seismic tomography results appear to be consistent with the findings of previous studies regard-  
342 ing the boundary between the Lachlan and Delamerian Orogens (Rawlinson et al., 2015; Rawlinson  
343 et al., 2016). The mantle model of Rawlinson et al. (2016), which covers mainland southeast Aus-  
344 tralia, shows a clear transition from high velocities in the west to lower velocities in the east. This  
345 same velocity transition is clearly imaged in our model (Fig. 11). Moreover, the location and dip di-  
346 rection of the velocity transition (marked “DLB” in section B-B' of Fig. 12) is consistent with the  
347 Moyston Fault at the surface (Cayley and Taylor, 1998; VandenBerg, 1999; Cayley et al., 2002),  
348 which is a widely accepted candidate for the Delamerian–Lachlan boundary in the crust. However,  
349 while the velocity transition in the mantle is unlikely to represent a continuation of this fault, it may

350 be the signature of an W-E contrast from Precambrian to Palaeozoic mantle lithosphere.

351 A long standing source of debate in southeast Australian tectonics is the possible connection be-  
 352 tween the mainland Delamerian Orogen and the Tyennan Orogen in Tasmania, where there have  
 353 been two schools of thought. Crawford et al. 2003 and Reed et al., 2002 proposed a model depicting  
 354 the two orogens connected directly. This connection is reinforced by several studies that have exam-  
 355 ined the age and geochemistry of various igneous rocks in both regions, and found strong similari-  
 356 ties. For example, Direen and Crawford (2003), have found paired suites of unusual ~580 Ma  
 357 olivine rich mafic volcanics, together with rare ~515 Ma boninites in both western Victoria and the  
 358 mainland Delamerian Orogen. However, subsequent studies (e.g. Cayley et al., 2011; Moore et al.,  
 359 2015, 2016) argued that the two orogens are not connected directly. In particular, Moore et al., 2015  
 360 found that the Tyennan and Delamerian Orogenies occurred at the same time but are displaced along  
 361 strike. In their model, the Tyennan Orogeny takes place further to the east and is controlled by the  
 362 master subduction zone to the Pacific plate.

363 In light of the above discussion, it is interesting to note that the velocity transition “DLB” observed  
 364 on the mainland does not show any extension southwards through Bass Strait to Tasmania. However,  
 365 one of the challenges in trying to interpret structure that was emplaced in the distant past from  
 366 present day geophysical images is that subsequent deformation and alteration will mask pre-existing  
 367 features and make any meaningful interpretation difficult. Notable tectonic events that post-date the  
 368 formation of the Delamerian and Lachlan Orogens include the break-up of Australia and Antarctica  
 369 and opening of the Tasman Sea, which resulted in the formation of the associated failed rift basins  
 370 that accommodate thick sedimentary sequences (Gaina et al., 1998). These events also resulted in  
 371 substantial thinning of the lithosphere towards the passive margin. The lower velocities observed be-  
 372 neath the Bass Strait-Tasmania region (Fig. 12 cross-section C-C'), may be a result of elevated tem-  
 373 peratures associated with the rifting and the presence of a thinner lithosphere, as well as the influ-  
 374 ence of the plume associated with the Cosgrove track. Hence the interpretation of Cayley et al. 2011  
 375 and Moore et al. 2015, 2016 may be consistent with our observation of the DLB not extending south  
 376 into Bass Strait, implying no direct connection between the Delamerian and Tyennan Orogens.

377 Recent studies have strengthened the argument for the presence of a Proterozoic continental  
 378 fragment, sourced from the break-up of Rodinia, beneath the Melbourne Zone in southern Victoria

379 (the so-called Selwyn Block), which extends south through Bass Strait to form the Precambrian  
380 basement of western Tasmania (Cayley, 2011; Moresi et al., 2014; Pilia et al., 2015a, 2015b; Moore  
381 et al., 2015, 2016). Following the earlier work of Cayley (2011), the existence of an entrained Pre-  
382 cambrian continental fragment has been reinforced by using 3-D geodynamic modeling (Moresi et  
383 al., 2014). This study suggests that an exotic continental fragment became entrained in the proto-Pa-  
384 cific convergent margin of eastern Australia, which resulted in a complex sequence of processes in-  
385 cluding differential subduction roll-back and southward transfer of material through continental  
386 transform faulting to form a large orocline that now underlies the Lachlan Orogen. The models illus-  
387 trate how significant curvature of the orogenic system develops, as well as the mechanism for tec-  
388 tonic escape of the back arc region.

389 Moore et al. (2015, 2016) provide robust geological and potential field evidence for the processes  
390 that led to the formation of Tasmania and how it is connected to mainland Australia. Their studies  
391 suggest that an extensional event along the Proto-Terra Australis margin began Rodinian breakup at  
392 approximately 830 Ma. As the extension continued, rifting took place along the Rodinian margin at  
393 around 600 Ma, which resulted in the separation of Laurentia, leaving vanDieland (comprising of  
394 the Selwyn Block, western Tasmania and the western part of the Bass Strait) attached to a thinned  
395 Gondwana margin. By 580 Ma vanDieland was completely rifted from Rodinia, forming three or  
396 four weakly connected cratonic ribbons separated by thinned continental or back-arc oceanic crust  
397 and a completely detached King Island. At the beginning of Ross Orogeny subduction, the rifted  
398 fragments of vanDieland drifted northwards at approximately 560 Ma. By 510 Ma or shortly there-  
399 after, trench advance during the Tyennan Orogeny caused closure between the cratonic blocks bring-  
400 ing most of them together. Finally, the micro continental ribbons became accreted within a closing  
401 back arc system and later, together with eastern Tasmania and the Lachlan Orogen, coalesced with  
402 the Gondwana Craton in the Middle Devonian. By 495 Ma all subduction processes had stalled and  
403 post collisional extension was underway. Moore et al. (2015, 2016) also demonstrate how the ac-  
404 creted vanDieland ribbons can be traced from present day Tasmania across Bass Strait into the Sel-  
405 wyn Block, thereby providing evidence that vanDieland is embedded in the Lachlan Orogen in  
406 southeast mainland Australia.

407 Pilia et al. (2015a) studied Bass Strait and adjoining land masses by applying a transdimensional

408 Bayesian inversion scheme to WOMBAT and BASS data to retrieve group velocity maps and 3-D  
409 shear wavespeed. The result is an image of the entire crust beneath Bass Strait that reveals a high ve-  
410 locity anomaly connecting southern Victoria and western Tasmania in the mid-lower crust, which is  
411 suggestive of a Proterozoic geological connection. This high velocity anomaly is consistent with re-  
412 cent gravity and magnetic maps and results from a seismic reflection survey through the Melbourne  
413 Zone in southern Victoria (Cayley et al., 2002, Cayley et al., 2011).

414 Our new model shows that high velocity anomalies in the upper mantle tend to underlie crust of Pre-  
415 cambrian continental origin, for example the Curnamona Province and Gawler Craton in Figure 12.  
416 Contrary to this, apart from the narrow sliver beneath the Melbourne zone, there is no evidence of a  
417 high velocity body in the upper mantle connecting mainland Australia and Tasmania. However, as  
418 noted previously, this does not necessarily rule out the existence of Precambrian continental mate-  
419 rial. Apart from the influence of recent plume activity, two possible explanations include delamina-  
420 tion of the mantle lithosphere beneath the fragment triggered by edge driven convection and shear  
421 driven upwelling (Rawlinson et al., 2017), or so-called rift-induced delamination (Wallner and  
422 Schmeling, 2010). Interestingly, mantle velocities below 200 km depth beneath Bass Strait (Fig. 12,  
423 cross-section C-C') are anomalously high compared with mantle beneath the Australian mainland,  
424 which potentially supports this hypothesis. However, the lack of any apparent uplift in Bass Strait,  
425 which would normally be a required response to the loss of a dense lithospheric mantle layer, means  
426 that this is not very likely. Furthermore, the deep high velocity zone is in part inherited from AuS-  
427 REM (Fig. 7d), which may not be well constrained in this region. A third possible explanation is  
428 that the micro-continent was subjected to intense lithospheric rifting during 250 Myr of Neoprotero-  
429 zoic extension which lead to Rodinian break-up, as suggested by Moore et al. (2015). This resulted  
430 in the development of continental ribbons (boudins), which by 510 Ma or shortly thereafter were  
431 brought together by the Tyennan Orogeny. This Rodinian extension is likely to have modified and  
432 thinned any high velocity mantle, resulting in a similar velocity signature to present day rifted mar-  
433 gins.

434 Previous studies (e.g. Pilia et al., 2015a, Rawlinson et al., 2016) have also suggested that any high  
435 velocity associated with a lithospheric keel beneath an entrained Precambrian continental fragment  
436 may have been overprinted by failed rifting associated with the break-up of Australia and Antarctica

437 and the opening of the Tasman Sea between 80 and 90 Ma (Gaina et al., 1998). Both of these events  
438 would have resulted in substantial thinning of the lithosphere in the Bass Strait region (marked 'BS'  
439 in Fig. 12, cross-section C-C'), and potentially elevated upper mantle temperatures. The rapid  
440 eastward decrease in upper mantle velocities towards the east coast of Australia (marked 'LTZ' Fig.  
441 12) is consistent with lithospheric thinning associated with the opening of the Tasman Sea. This  
442 change is due to the proximity of the passive margin and may be accentuated by the presence of  
443 asymmetric rifting, with the upper-plate margin underlying the Australian east coast (Lister et al.,  
444 1986; Lister and Etheridge, 1989; Lister et al., 1991).

## 445 **5. Conclusions**

446 In this study, a P-wave velocity model of the crust and upper mantle was used to investigate the  
447 broad-scale geology of the Bass Strait region. The inversion of teleseismic arrival time residuals  
448 from WOMBAT and BASS transportable array data for mantle velocity variations was improved by  
449 embedding a detailed ambient noise crustal model and AuSREM Moho and mantle velocity  
450 variations in the starting model. Resolution tests show that the new model of the Bass Strait region  
451 is generally well constrained by the data set beneath the horizontal bounds of the array, although  
452 there is a lack of coverage beneath the centre of Bass Strait to a depth of approximately 100 km due  
453 to the use of only land-based stations. North of Victoria, the pattern of anomalies is consistent with  
454 previous studies that have exploited the WOMBAT teleseismic dataset. We also image a distinct low  
455 velocity zone beneath the NVP in western Victoria, and show that (i) it is restricted to the upper  
456 mantle, and appears to die out at around 150 km depth; and (ii) it lies at the northern end of a  
457 pervasive low velocity zone in the upper mantle that stretches between Victoria and Tasmania. As  
458 such, we do not find any evidence to support the existence of a Precambrian microcontinent that  
459 joins Tasmania to the mainland, as has been suggested in recent studies. However, we cannot rule  
460 out the possibility that hyper-extension during Rodinian break-up, failed rifting in Bass Strait  
461 associated with the separation of Australia and Antarctica, the opening of the Tasman Sea and  
462 mantle sources of recent intra-plate volcanism may have conspired to reduce seismic wavespeeds  
463 via processes such as lithospheric stretching, delamination, changes in bulk composition and  
464 heating.

465

## 466 **Acknowledgments**

467 We thank many land owners and field team members from mainland Australia and Tasmania.  
468 Particular thanks to Armando Arcidiaco and Qi Li from ANU for assistance with the collection and  
469 archiving of the data used in this study. ARC grants DP120103673, LE120100061, LP110100256  
470 and DP0986750 were instrumental in supporting the WOMBAT and BASS deployments.

## 472 **References**

- 473 Achauer, U., 1994. New ideas on the Kenya rift based on the inversion of the combined dataset of  
474 the 1985 and 1989/90 seismic tomography experiments. *Tectonophysics* 236, 305 – 329.
- 475
- 476 Aki, K., Christossffersson A., Husebye, E. S., 1977. Determination of the three dimensional seismic  
477 structure of the lithosphere. *J. Geophys. Res.* 82, 277–296.
- 478
- 479 Benson, G. D., Ritzwoller, M. H., Shapiro, N. M., 2008. Broadband ambient noise surface wave to-  
480 mography across the United States. *J. Geophys. Res.* 113, [http://dx.doi.org/](http://dx.doi.org/10.1029/2007JB005248)  
481 10.1029/2007JB005248.
- 482 Black, L.P., Calver, C.R., Seymour, D.B., Reed, A., 2004. SHRIMP U-Pb detrital zircon ages from  
483 Proterozoic and Early Palaeozoic sandstones and their bearing on the early geological evolution  
484 of Tasmania. *Australian Journal of Earth Sciences* 51, 885-900.
- 485
- 486 Boger, S., and Miller, J., 2004. Terminal suturing of Gondwana and the onset of the Ross  
487 Delamerian Orogeny: the cause and effect of an Early Cambrian reconfiguration of plate  
488 motions. *Earth and Planetary Science Letters* 219, 35–48.
- 489 Cawood, P.A., 2005. Terra Australis Orogen: Rodinia breakup and development of the Pacific and  
490 Iapetus margins of Gondwana during the Neoproterozoic and Paleozoic. *Earth-Science Reviews*  
491 69, 249–279. [http://dx.doi.org/ 10.1016/j.earscirev.2004.09.001](http://dx.doi.org/10.1016/j.earscirev.2004.09.001).
- 492 Cayley, R. A., Taylor, D. H., 1998. The Lachlan margin Victoria: the Moyston Fault, a newly  
493 recognised terrane boundary. *Geol. Soc. Aust. Abstr.* 49, 73.
- 494 Cayley, R., Taylor, D. H., VandenBerg, A. H. M., Moore, D. H., 2002. Proterozoic–Early  
495 Palaeozoic rocks and the Tyennan Orogeny in central Victoria: the Selwyn Block and its tectonic

496 implications. *Aust. J. Earth Sci.* 49, 225–254.

497

498 Cayley, R., 2011. Exotic crustal block accretion to the eastern Gondwanaland margin in the Late  
 499 Cambrian Tasmania, the Selwyn Block, and implications for the Cambrian–Silurian evolution of  
 500 the Ross, Delamerian, and Lachlan orogens. *Gondwana Research* 19, 628–649. [http://dx.doi.org/](http://dx.doi.org/10.1016/j.gr.2010.11.013)  
 501 10.1016/j.gr.2010.11.013.

502 Cayley, R., Korsch, R. J., Moore, D. H., Costelloe, R.D., Nakamura, A., Willman, C. E., Rawlin, T.  
 503 J., Morand, V. J., Skladzien, P. B., O’Shea, P. J., 2011. Crustal architecture of central Victoria:  
 504 results from the 2006 deep crustal reflection seismic survey. *Australian Journal of Earth Sciences*  
 505 59, 113–156.

506 Clifford, P., Greenhalgh, S., Houseman, G., Graeber, F., 2008. 3-d seismic tomography of the Ade-  
 507 laide fold belt, *Geophys. J. Int.* 172, 167–186.

508 Crowder, E., Rawlinson, N., Pilia, S., Cornwell, D. G. and Reading, A. M., 2019. Transdimensional  
 509 ambient noise tomography of Bass Strait, southeast Australia, reveals the sedimentary basin and  
 510 deep crustal structure beneath a failed continental rift. *Geophysical Journal International*, 217,  
 511 970–987.

512

513 Crawford, A. J., Meffre, S., and Symonds, P. A., 2003. 120 to 0 Ma tectonic evolution of the south-  
 514 west Pacific and analogous geological evolution of the 600 to 220 Ma Tasman Fold Belt System.  
 515 In: Hillis R. R. & Mülle R. D. eds. *Evolution and dynamics of the Australian Plate*, 383–404.  
 516 Geological Society of Australia Special Publication 22 and Geological Society of America Spe-  
 517 cial Publicaion 372.

518

519 Dalton, C. A., Faul, U. H., 2010. The oceanic and cratonic upper mantle: clues from joint interpreta-  
 520 tion of global velocity and attenuation models. *Lithos* 120, 160–172.

521 Davies, D. R., Rawlinson, N., Iaffaldano, N., Campbell, I. H., 2015. Lithospheric controls on  
 522 magma composition along Earth's longest continental hotspot track. *Nature* 525, 511–514.

523 Day, A. J., Peirce, C., Sinha, M. C., 2001. Three-dimensional crustal structure and magma chamber  
 524 geometry at the intermediate spreading, back-arc Valu Fa Ridge, Lau Basin—results of a wide-  
 525 angle seismic tomographic inversion. *Geophysical J. Int.* 146, 31–52.

526

527 de Kool, M., Rawlinson, N., Sambridge, M., 2006. A practical grid based method for tracking multi-



528 ple refraction and reflection phases in 3D heterogeneous media. *Geophysical J. Int.* 167, 253–  
529 270.

530 Direen, N. G., Crawford, A.J., 2003. The Tasman Line: where is it, what is it, and is it Australia's  
531 Rodinian breakup boundary? *Aust. J. Earth Sci.* 50, 491–502.

532

533 Drummond, B., Barton, T., Korsch, R., Rawlinson, N., Yeates, A., Collins, C., Brown, A., 2000.  
534 Evidence for crustal extension and inversion in eastern Tasmania, Australia, during the  
535 Neoproterozoic and Early Palaeozoic. *Tectonophysics* 329, 1–21. [http://dx.doi.](http://dx.doi.org/10.1016/S0040-1951(00)00185-2)  
536 [org/10.1016/S0040-1951\(00\)00185-2](http://dx.doi.org/10.1016/S0040-1951(00)00185-2).

537

538 Fishwick, S., Rawlinson, N., 2012. 3-D structure of the Australian lithosphere from evolving seis-  
539 mic datasets. *Aust. J. Earth Sci.* 59, 809–826.

540 Gaina, C., Müller, D., Royer, J. -Y., Stock, J., Hardebeck, J., Symonds, P., 1998. The tectonic his-  
541 tory of the Tasman Sea, a puzzle with 13 pieces. *J. Geophys. Res.* 103, 12,413–12,433.

542 Glahn, A., and Granet, M., 1993. Southern Rhine Graben: small wavelength tomographic study and  
543 implications for the dynamic evolution of the graben, *Geophys. J. Int.* 113, 399–418.

544

545 Glen, R. A., 2005. The Tasmanides of Eastern Australia. In: Vaughan, A.P.M., Leat, P.T.,  
546 Pankhurst, R.J. (Eds.), *Terrane Processes at the Margins of Gondwana*. Geological Society,  
547 London, 23–96.

548

549 Graeber, F. M. and Asch, G., 1999. Three-dimensional models of P wave velocity and P-to-S  
550 velocity ratio in the southern central Andes by simultaneous inversion of local earthquake data:  
551 *J. Geophys. Res.* 104, 20,237–20,256.

552

553 Graeber, F. M., Houseman, G.A., Greenhalgh, S.A., 2002. Regional teleseismic tomography of the  
554 western Lachlan Orogen and the Newer Volcanics Province, southeast Australia. *Geophysical*  
555 *Journal International* 149, 249–266.

556

557 Hand, M., Reid, A., Szpunar, M., Direen, N., Wade, B., Payne, J., Barovich, K., 2008. Crustal ar-  
558 chitecture during the early Mesoproterozoic Hiltaba-related mineralisation event: are the Gawler  
559 Range Volcanics a foreland basin fill? *MESA J.* 51, 19–24.

560 Humphreys, E. D., and Clayton, R. W., 1990. Tomographic image of the southern California

561 mantle. *J. Geophys. Res.* 95, 19,725 – 19,746.

562

563 Jones, I., and Verdel, C., 2015. Basalt distribution and volume estimates of Cenozoic volcanism in  
 564 the Bowen Basin region of eastern Australia: Implications for a waning mantle plume.  
 565 *Australian Journal of Earth Sciences* 62:2, 255-263, doi: 10.1080/08120099.2015.997796.

566

567 Kennett, B. L. N., Sambridge, M. S., Williamson, P. R., 1988. Subspace methods for large scale  
 568 inverse problems involving multiple parameter classes. *Geophysical. J. Int.* 94, 237–247.

569

570 Kennett B. L. N., Fichtner, A., Fishwick, S., Yoshizawa, K., 2013. Australian seismological refer-  
 571 ence model (AuSREM): mantle component. *Geophys J. Int.* 192, 871–887.

572 King, S. D., and Anderson, D. L., 1998. Edge-Driven Convection. *Earth Planet. Sci. Lett.* 160, 289-  
 573 296.

574 King, S. D., and Ritsema, J., 2000. African hotspot volcanism: small-scale convection in the upper  
 575 mantle beneath cratons, *Science* 290, 1137-1140.

576 Leaman, D., Baillie, P., Powell, C.M., 1994. Precambrian Tasmania: a thin-skinned devil.  
 577 *Exploration Geophysics* 25, 19–23. <http://dx.doi.org/10.1071/EG994019>.

578 Lévêque, J. J., Rivern, L., and Wittlinger, G., 1993. On the use of the checkerboard test to assess the  
 579 resolution of tomographic inversions. *Geophys. J. Int.* 115, 313 – 318.

580

581 Lippitsch, R., Kissling, E. and Ansorge, J., 2003. Upper mantle structure beneath the Alpine orogen  
 582 from high-resolution teleseismic tomography. *J. Geophys. Res.* 108(B8), 2376,  
 583 doi:10.1029/2002JB002016.

584

585 Lister, G. S., Ethridge, M. A., Symonds, P. A., 1986. Detachment faulting and the evolution of pas-  
 586 sive continental margins: *Geology* 14, 246–250.

587 Lister, G. S., Etheridge, M. A., 1989. Detachment models for uplift and volcanism in the Eastern  
 588 Highlands, and their application to the origin of passive margin mountains. In: Johnson, R.W.  
 589 (Ed.), *Intraplate Volcanism in Eastern Australia and New Zealand*. Cambridge University Press,  
 590 New York, 297–312.

591 Lister, G. S., Ethridge, M. A., Symonds, P. A., 1991. Detachment models for the formation of pas-

592 sive continental margins. *Tectonics* 10, 1038–1064.

593 Meffre, S., Direen, N.G., Crawford, A. J., Kamenetsky, V. 2004. Mafic volcanic rocks on King  
594 Island, Tasmania: Evidence for 579 Ma break-up in east Gondwana. *Precambrian Research* 135,  
595 177-191.

596 Moore, D.H., Betts, P.G. & Hall, M., 2015. "Fragmented Tasmania: the transition from Rodinia to  
597 Gondwana", *Australian Journal of Earth Sciences* 62, 1-35.

598 Moore, D.H., Betts, P.G. & Hall, M., 2016. Constraining the VanDieland microcontinent at the edge  
599 of East Gondwana, Australia. *Tectonophysics* 687, 158-179.

600

601 Moresi, L., Betts, P. G., Miller, M. S., Cayley, R. A., 2014. Dynamics of continental accretion.  
602 *Nature* 508, 245–248.

603 Morse, M., Gibson, G., Mitchell, C., 2009. Basement constraints on offshore basin architecture as  
604 determined by new aeromagnetic data acquired over Bass Strait and western margin of  
605 Tasmania. *ASEG Extended Abstracts 2009*, 1–9, <http://dx.doi.org/10.1071/ASEG2009ab042>.

606 Oncescu, M. C., Burlacu, V., Anghel, M., Smalbergher, V., 1984, Three-dimensional P-wave  
607 velocity image under the Carpathian Arc. *Tectonophysics* 106, 305–319.

608 O'Sullivan, P., Mitchell, M., O'Sullivan, A., Kohn, B., Gleadow, A., 2000. Thermotectonic history  
609 of the Bassian Rise, Australia: Implications for the breakup of eastern Gondwana along  
610 Australia's southeastern margins. *Earth and Planetary Science Letters* 182, 31–47.  
611 [http://dx.doi.org/10.1016/S0012-821X\(00\)00232-6](http://dx.doi.org/10.1016/S0012-821X(00)00232-6).

612 Pilia, S., Rawlinson, N., Green, N. G., Reading, A. M., Cayley, R., Pryer, L., Arroucau, P., and  
613 Duffet, M., 2015a. Linking mainland Australia and Tasmania using ambient seismic noise  
614 tomography: Implications for the tectonic evolution of the east Gondawana margin. *Gondwana*  
615 *Research* 28, 1212-1227.

616 Pilia, S., Rawlinson, N., Cayley, R. A., Musgrave, R., Reading, A. M., Direen, N. G., Young, M.  
617 K., 2015b. Evidence of micro-continent entrainment during crustal accretion. *Sci. Rep.* 5.  
618 <http://dx.doi.org/10.1038/srep/08218>.

619 Rawlinson, N. and Sambridge, M., 2003. Irregular interface parameterization in 3-D wide-angle  
620 seismic traveltimes tomography. *Geophysical Journal International* 155, 79-92.

621 Rawlinson, N. and Kennett, B. L. N., 2004. Rapid estimation of relative and absolute delay times  
622 across a network by adaptive stacking. *Geophysical Journal International* 157, 332–340.

623 Rawlinson N, and Sambridge M., 2004a. Multiple reflection and transmission phases in complex  
624 layered media using a multistage fast marching method. *Geophysics* 69,1338–1350.

625 Rawlinson, N., and Sambridge, M., 2004b. Wavefront evolution in strongly heterogeneous layered  
626 media using the fast marching method. *Geophysical Journal International* 156, 631–647.

627 Rawlinson, N., Reading, A., Kennett, B., 2006. Lithospheric structure of Tasmania from a novel  
628 form of teleseismic tomography: *Journal of Geophysical Research* 111, B02301.  
629 <http://dx.doi.org/10.1029/2005JB003803>  
630

631 Rawlinson, N., Urvoy, M., 2006. Simultaneous inversion of active and passive source datasets for  
632 3-D seismic structure with application to Tasmania. *Geophys. Res. Lett.* 33, L24313.  
633

634 Rawlinson, N., Kennett, B., 2008. Teleseismic tomography of the upper mantle beneath the  
635 southern Lachlan Orogen, Australia. *Physics of the Earth and Planetary Interiors* 167, 84–97.  
636 <http://dx.doi.org/10.1016/j.pepi.2008.02.07>.  
637

638 Rawlinson, N., Pozgay, S., Fishwick, S., 2010. Seismic tomography: a window into deep Earth.  
639 *Phys. Earth Planet. Inter.* 178, 101–135.

640 Rawlinson, N., Kennett, B., Vanacore, E., Glen, R., Fishwick, S., 2011. The structure of the upper  
641 mantle beneath the Delamerian and Lachlan orogens from simultaneous inversion of multiple  
642 teleseismic datasets. *Gondwana Res.* 19, 788–799.

643 Rawlinson, N., Fishwick, S., 2012. Seismic structure of the southeast Australian lithosphere from  
644 surface and body wave tomography. *Tectonophysics* 572, 111–122.

645 Rawlinson, N., Kennett, B. L. N., Salmon, M., Glen, R. A., 2015. Origin of lateral heterogeneities  
646 in the upper mantle beneath South-East Australia from seismic tomography. In: Khan, A.,  
647 Deschamps, F. (Eds.), *The Earth's Heterogeneous Mantle: A Geophysical, Geodynamical and*  
648 *Geochemical Perspective*, Springer Geophysics. Springer, 47–78.

649 Rawlinson, N., Pilia, S., Young, M. Salmon, M., Yang, Y., 2016. Crust and upper mantle structure  
650 beneath southeast Australia from ambient noise and teleseismic tomography. *Tectonophysics*

651 689, 143-156. <http://dx.doi.org/10.1016/j.tecto.2015.11.034>.

652 Rawlinson, N., Spakman, W., 2016. On the use of sensitivity test in seismic tomography. *Geophys.*  
653 *J. Int.* 205, 1221–1243.

654 Rawlinson, N., Davies, D. R., Pilia, S., 2017. The mechanisms underpinning Cenozoic intraplate  
655 volcanism in eastern Australia. Insights from seismic tomography and geodynamic modeling.  
656 *Geophysical Research Letters* 44 (19), 9,681-9,690.

657

658 Reed A. R., Calvert C., Bottrill, R. S., 2002. Palaeozoic suturing of eastern and western Tasmania in  
659 the west Tamar region: Implications for the tectonic evolution of southeast Australia. *Australian*  
660 *Journal of Earth Sciences* 49, 809–830.

661 Ritsema, J., A. Nyblade, A., Owens, T. J., Langston, C. A., VanDecar, J. C., 1998. Upper mantle  
662 seismic velocity structure beneath Tanzania, east Africa: Implications for the stability of cratonic  
663 lithosphere. *J. Geophys. Res.* 103, 21201–21213.

664 Salmon, K., Kennett, B. L. N., Saygin, E., 2013. Australian Seismological Reference Model (AuS-  
665 REM): crustal component. *Geophys. J. Int.* 192, 190–206.

666 Sethian, J. A., 1996. A fast marching level set method for monotonically advancing fronts. *Proc.*  
667 *Natl. Acad. Sci.* 93, 1591–1595.

668 Sethian, J. A., and Popovici, A. M., 1999. 3-D traveltimes computation using the fast marching  
669 method. *Geophysics* 64, 516 – 523.

670

671 Steck, L. K., Thurber, C. H., Fehler, M., Lutter, W. J., Roberts, P. M., Baldridge, W. S., Stafford, D.  
672 G., and Sessions, R., 1998. Crust and upper mantle P wave velocity structure beneath Valles  
673 caldera, New Mexico: Results from the Jemez teleseismic tomography experiment. *J. Geophys.*  
674 *Res.* 103, 24,301 – 24,320.

675

676 Sun, W., and Kennett, B., 2016. Uppermost mantle structure of the Australian continent from Pn  
677 traveltimes tomography, submitted to *Journal of Geophysical Research: solid earth* 121(3), 2004-  
678 2019.

679

680 VandenBerg, A. H. M., 1999. Timing of orogenic events in the Lachlan Orogen. *Aust. J. Earth Sci.*  
681 46, 691–701.

682 Wallner, H., and Schmeling, H., 2010. Rift induced delamination of mantle lithosphere and crustal  
683 uplift: a new mechanism for explaining Rwenzori Mountains' extreme elevation? *International*  
684 *Journal of Earth Sciences* 99, 1511–1524.

685

686 Wei, Z., Kennett, B. L. N., Sun, W., 2018. Sn-wave velocity structure of the uppermost mantle  
687 beneath the Australian continent, *Geophys. J. Int.* 213, 2071–2084.

688

689 White, L., Gibson, G., Lister, G., 2013. A reassessment of paleogeographic reconstructions of  
690 eastern Gondwana: bringing geology back into the equation. *Gondwana Research* 24, 984–998.  
691 <http://dx.doi.org/10.1016/j.gr.2013.06.00>

692

693 Yao, H., van der Hilst, R. D., de Hoop, M. V., 2006. Surface-wave array tomography in SE Tibet  
694 from ambient seismic noise and two-station analysis - I. Phase velocity maps. *Geophys. J. Int.*  
695 166, 732–744.

696 Young, M. K., Rawlinson, N., Arroucau, P., Reading, A.M., Tkalčić, H., 2011. High-frequency am-  
697 bient noise tomography of southeast Australia: new constraints on Tasmania's tectonic past. *Geo-*  
698 *phys. Res. Lett.* 38, L13313. <http://dx.doi.org/10.1029/2011GL047971>.

699 Young, M. K., Rawlinson, N., Bodin, T., 2013a. Transdimensional inversion of ambient seismic  
700 noise for 3D shear velocity structure of the Tasmanian crust. *Geophysics* 78. [http://dx.](http://dx.doi.org/10.1190/geo2012-0356.1)  
701 [doi.org/10.1190/geo2012-0356.1](http://dx.doi.org/10.1190/geo2012-0356.1).

702 Young, M. K., Cayley, R. A., McLean, M. A., Rawlinson, N., Arroucau, P., Salmon, M., 2013b.  
703 Crustal structure of the east Gondwana margin in southeast Australia revealed by transdimen-  
704 sional ambient seismic noise tomography. *Geophys. Res. Lett.* 40, 4266–427.

705

706

707

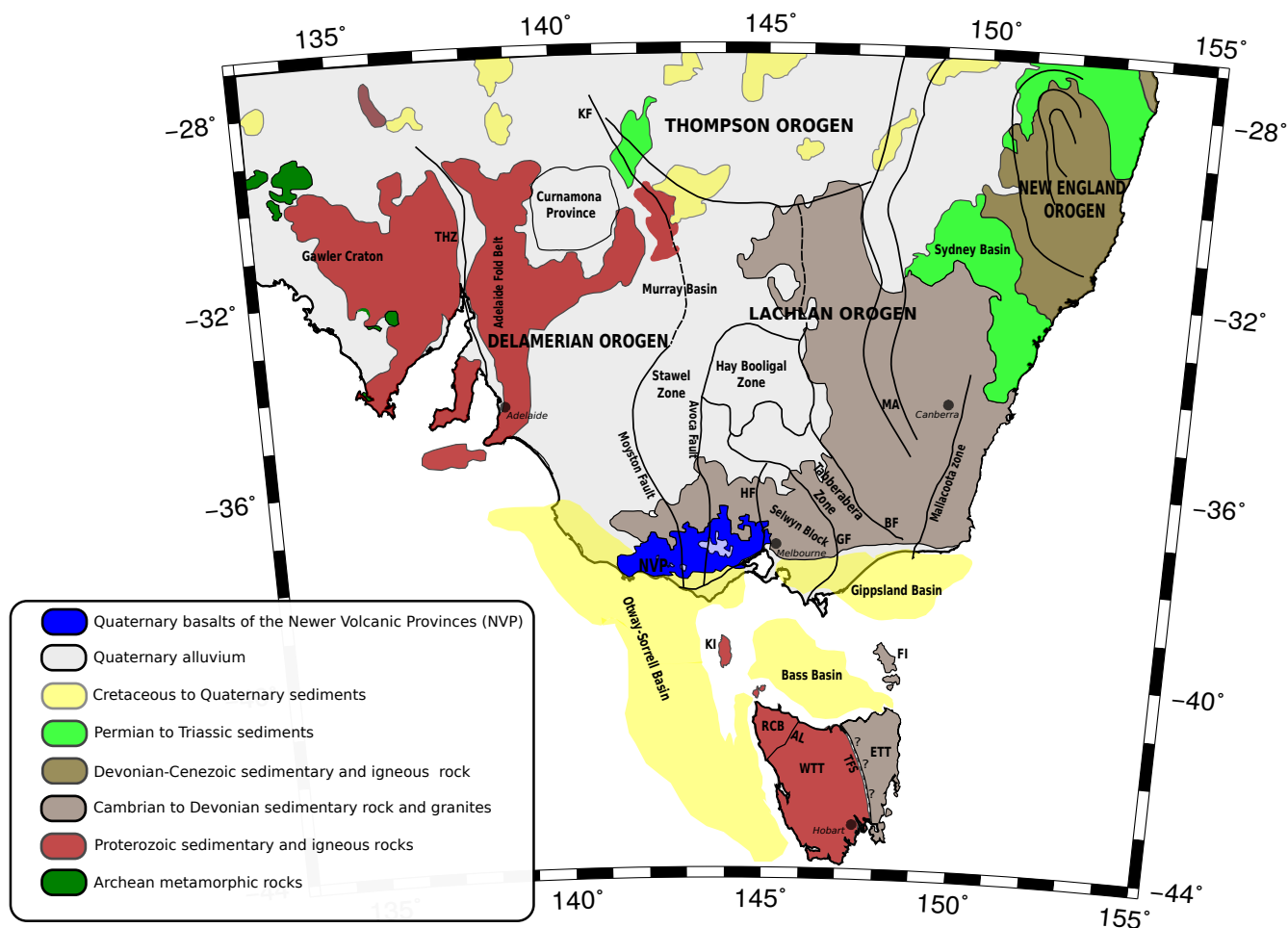


**Fig. 1:** Simplified geological map of southeastern Australia showing observed and inferred geological boundaries and main tectonic features mentioned in the text. Thick black lines show locations of structural boundaries. KF = Koonenberry Fault; HF = Heathcote Fault; GF = Governor Fault; BF = Bootheragandra Fault; THZ = Torrens Hinge Zone; NVP = Newer Volcanic Province; MA = Macquarie Arc; KI = King Island and FI = Flinders Island in Bass Strait; WTT = Western Tasmania Terrane; ETT = Eastern Tasmania Terrane; AL = Arthur Lineament; TFS = Tamar Fracture System and RCB = Rocky Cape Block.

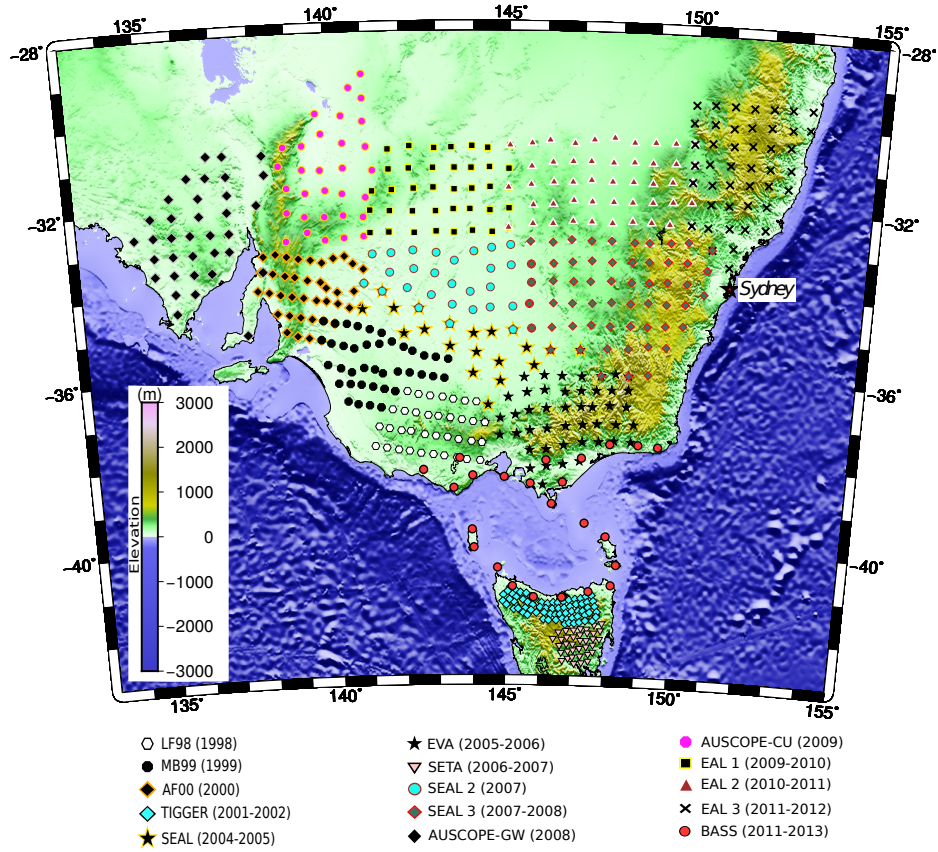


**Fig. 2:** Topographic/bathymetric map of the study area showing locations of the fifteen different arrays represented by different symbols.



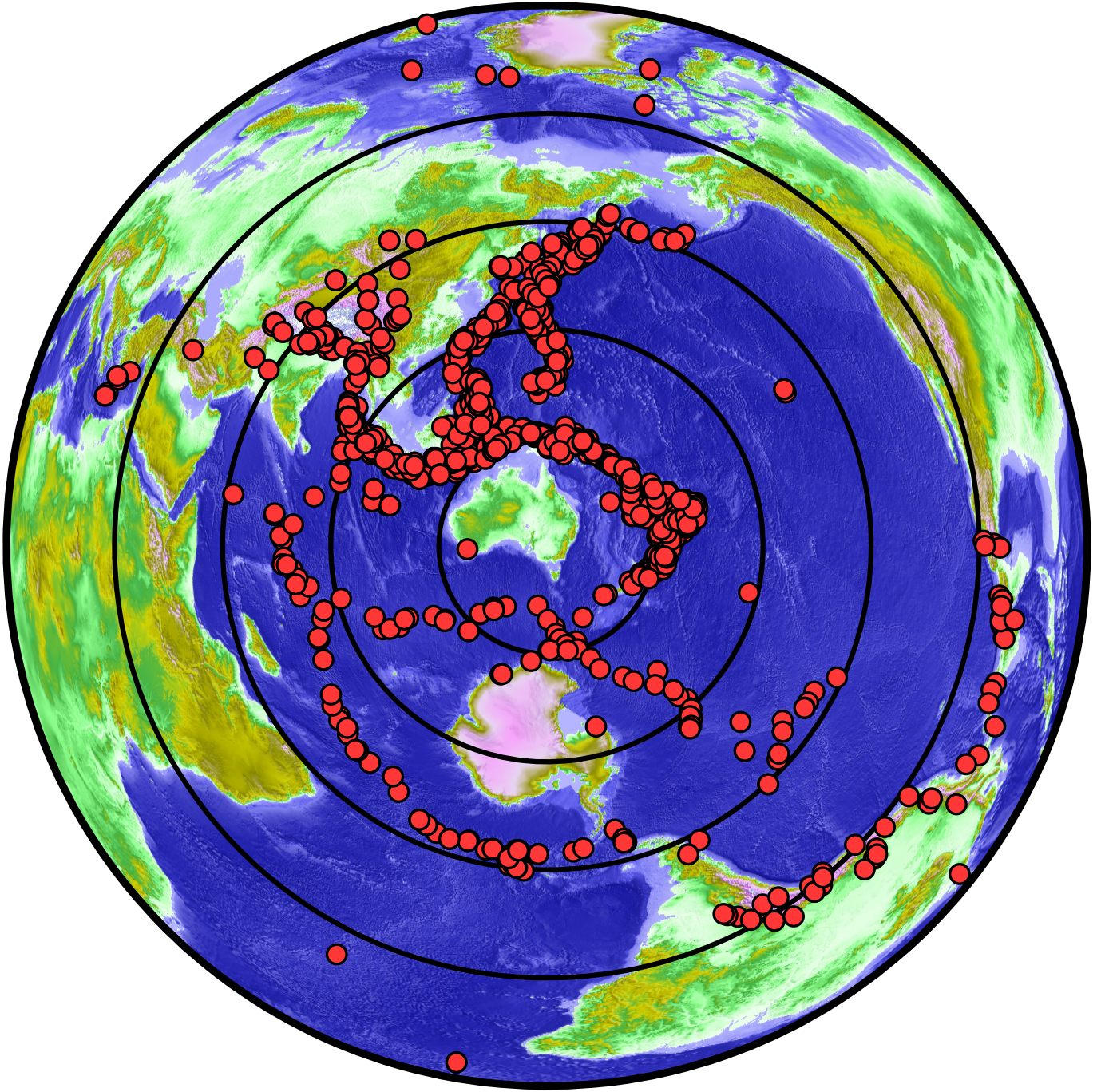


**Fig. 3:** Distribution of teleseismic events used to constrain the 3-D P wave velocity model. Concentric circles are plotted at  $30^\circ$  intervals from the centre of Bass Strait.

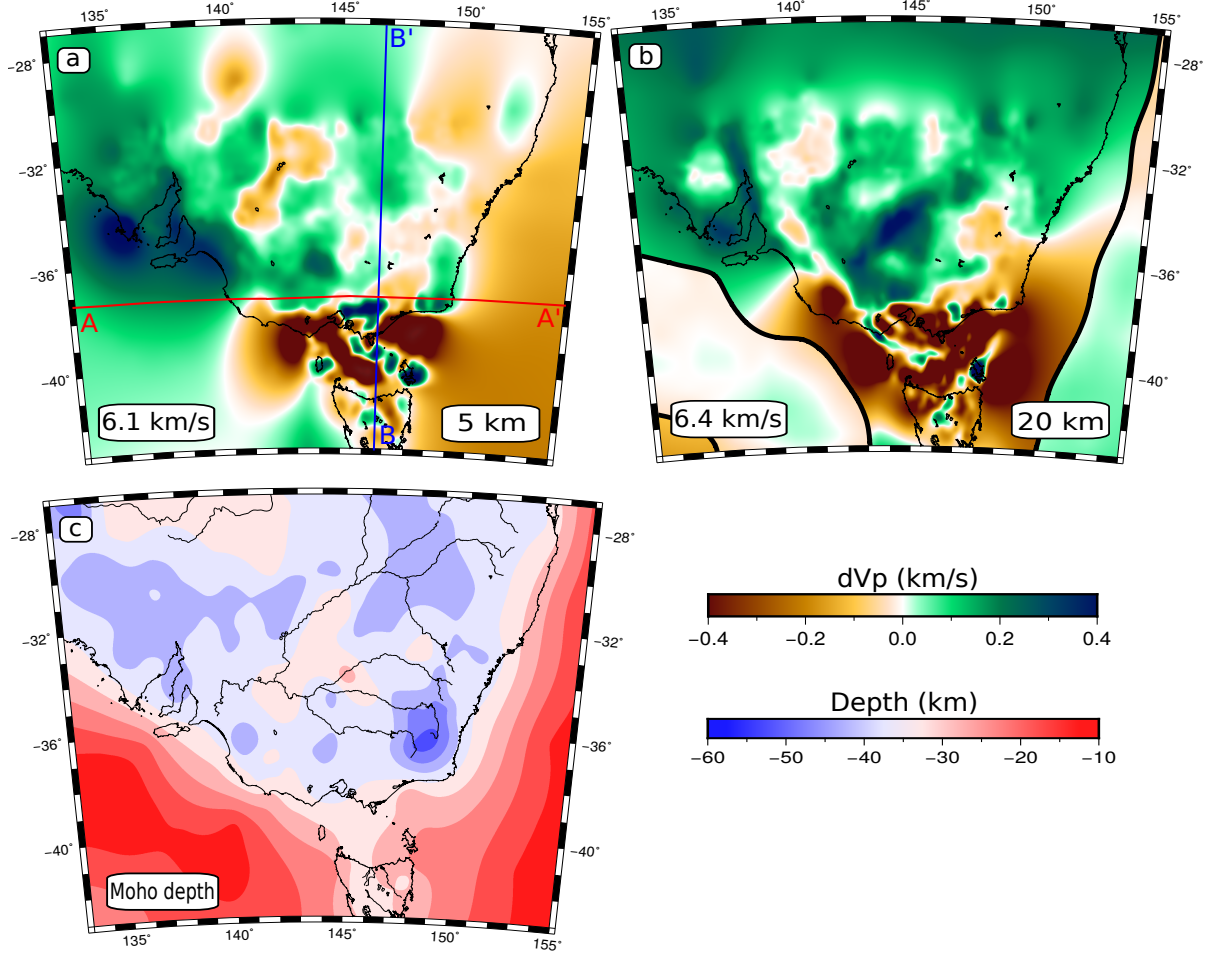


**Fig. 4:** (a,b) Two depth slices through the new ambient noise crustal model at 5 km and 20 km depth. Since it is the relative velocity variations that are important for teleseismic tomography, perturbations from a laterally averaged depth-dependent 1-D version of the model are shown in the bottom left hand corner of (a,b). Thick black lines (see 20 km depth slice in (b)) denote the intersection of the depth slice with the Moho. (c) AuSREM Moho depth model for southeast Australia, which is also used in the starting model of the teleseismic tomography. We have converted the original S-wave velocity model to P-wave velocity, which is what is shown here.

Fiji Islands; 16/05/2012; Mw=6.6

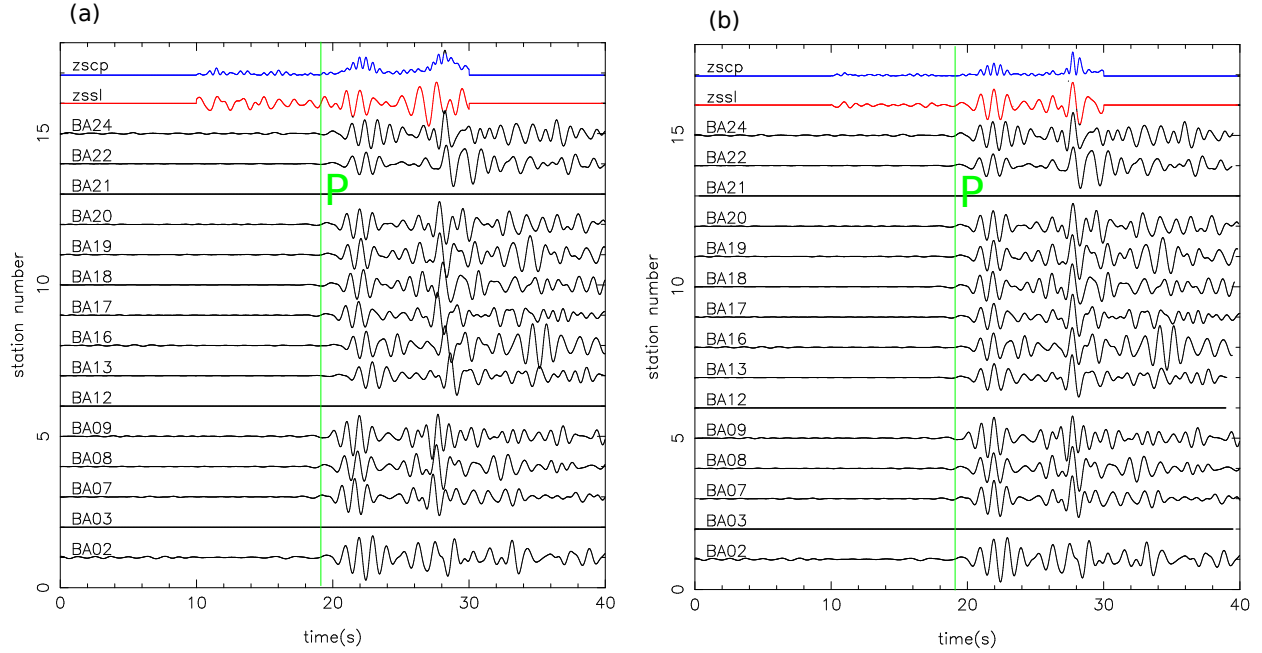


**Fig. 5:** Example of adaptive stacking of recorded P waves at BASS stations. (a) are the filtered traces before stacking; (b) the filtered traces after stacking. The top blue and red coloured traces are the quadratic stack (zscp) and linear stack (zssl) respectively. The vertical green lines indicate predictions from the global reference model ak135, to which all traces have been aligned in (b).

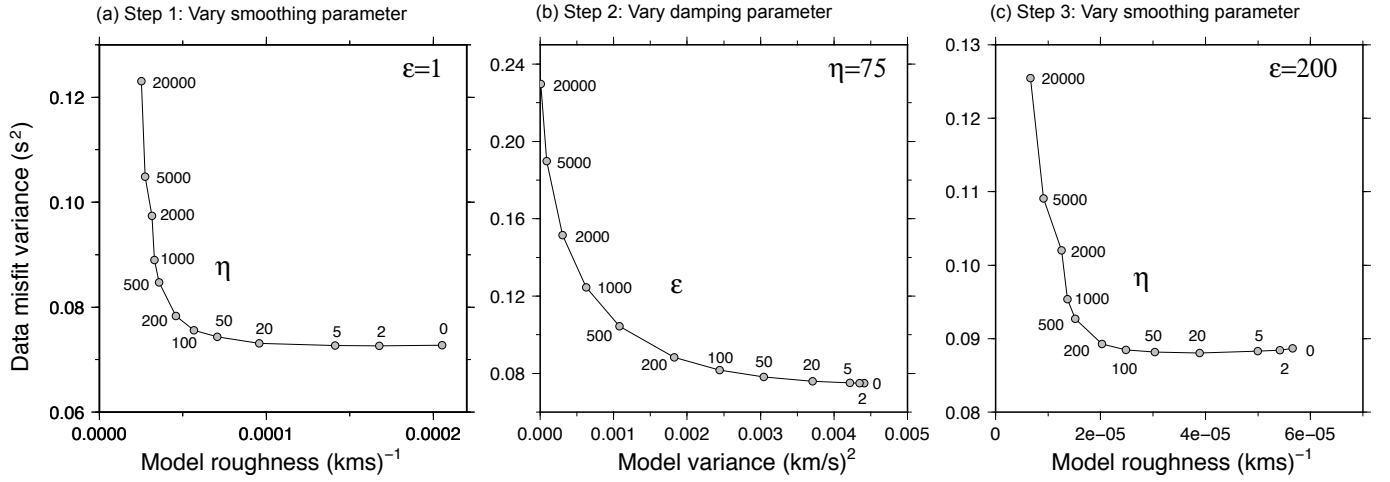


**Fig. 6:** Trade-off curve used to find optimum damping and smoothing parameters. (a) Vary smoothing parameter while holding damping parameter fixed at  $\varepsilon = 1$ . (b) Vary damping parameter while holding smoothing parameter fixed at  $\eta = 75$ . (c) Vary  $\eta$  while holding the damping parameter fixed at the new value of  $\varepsilon = 200$ . In all the three cases,  $\varepsilon = \eta = 200$  appear to be an acceptable choice.



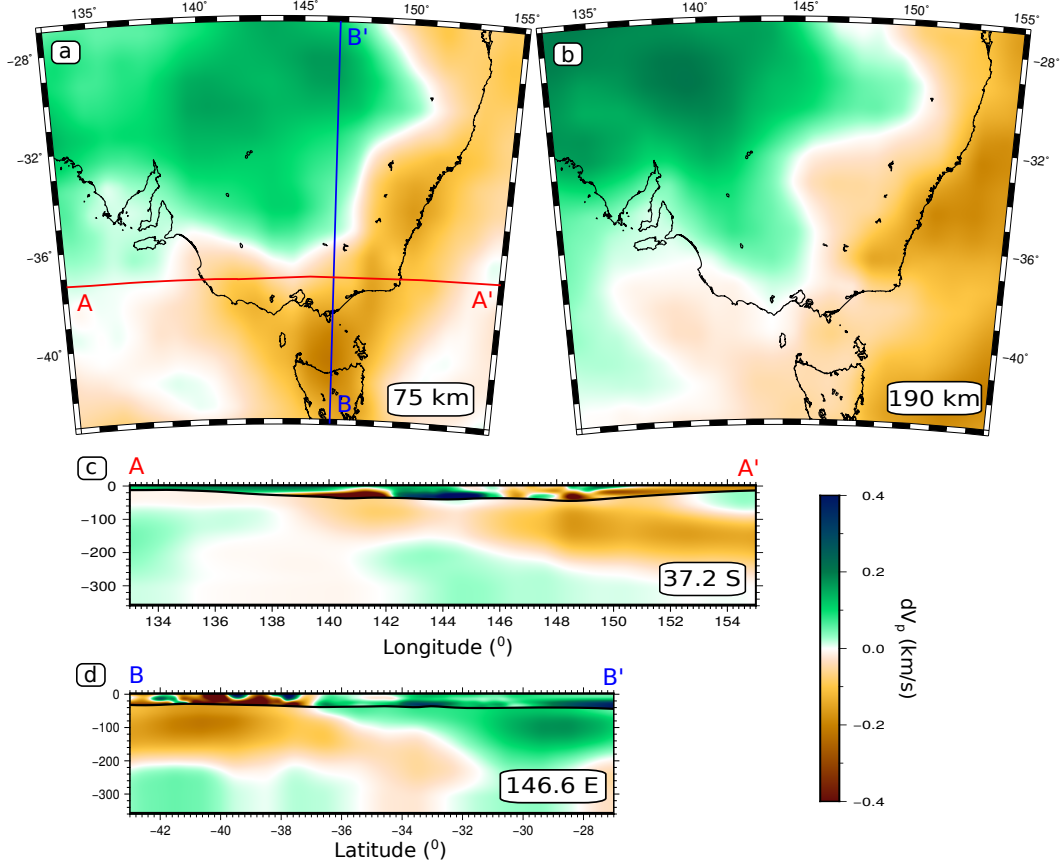


**Fig. 7:** A selection of slices through the starting model used for teleseismic tomography. (a) 75 km depth slice; (b) 190 km depth slice; (c) EW cross-section at 37.2°S; (d) NS cross-section at 146.6°E. In all cases, velocities are plotted relative to a reference one-dimensional model. The horizontal red line and vertical blue line in (a) denote the cross-section locations of (c) and (d) respectively.

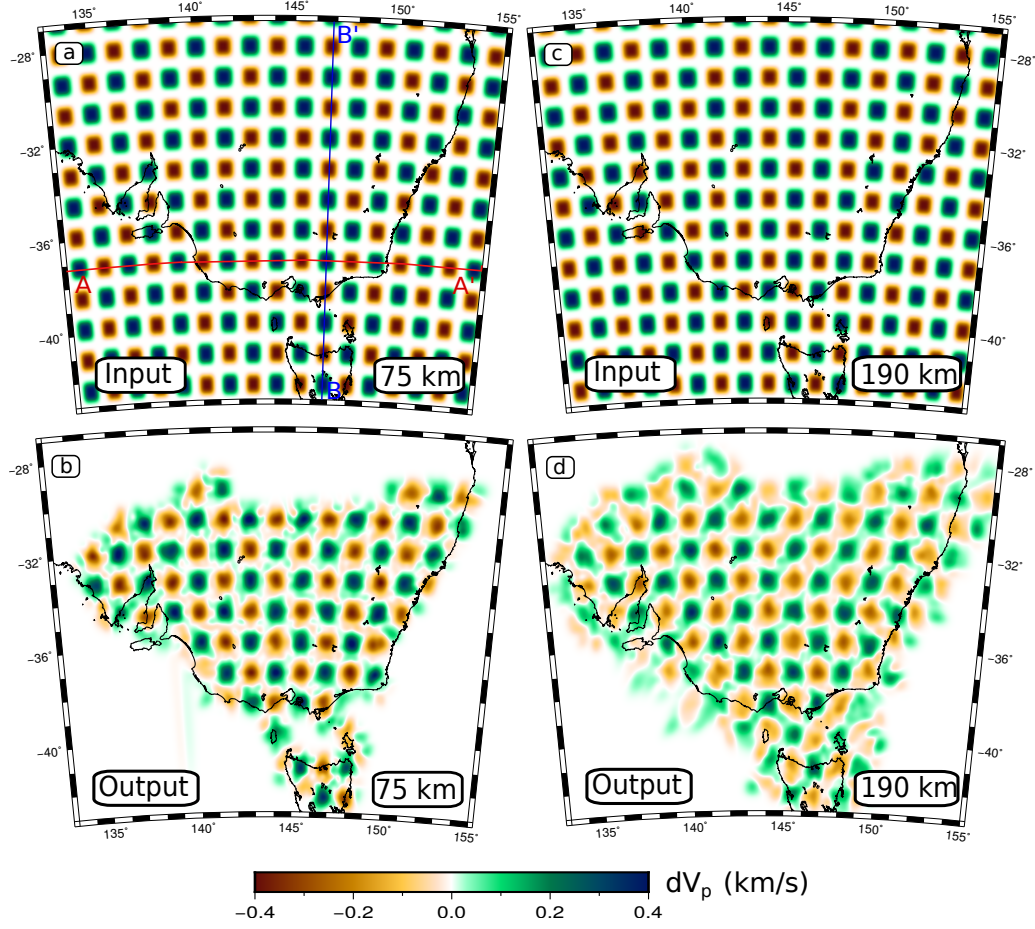


**Fig. 8:** Depth sections illustrating the synthetic resolution test results. (a) Input test model at 75 km depth; (b) recovered model at 75 km depth; (c) input test model at 190 km depth; (d) recovered model at 190 km depth. The horizontal red and vertical blue lines in (a) denote the cross-section locations of Fig. 9a and b respectively.

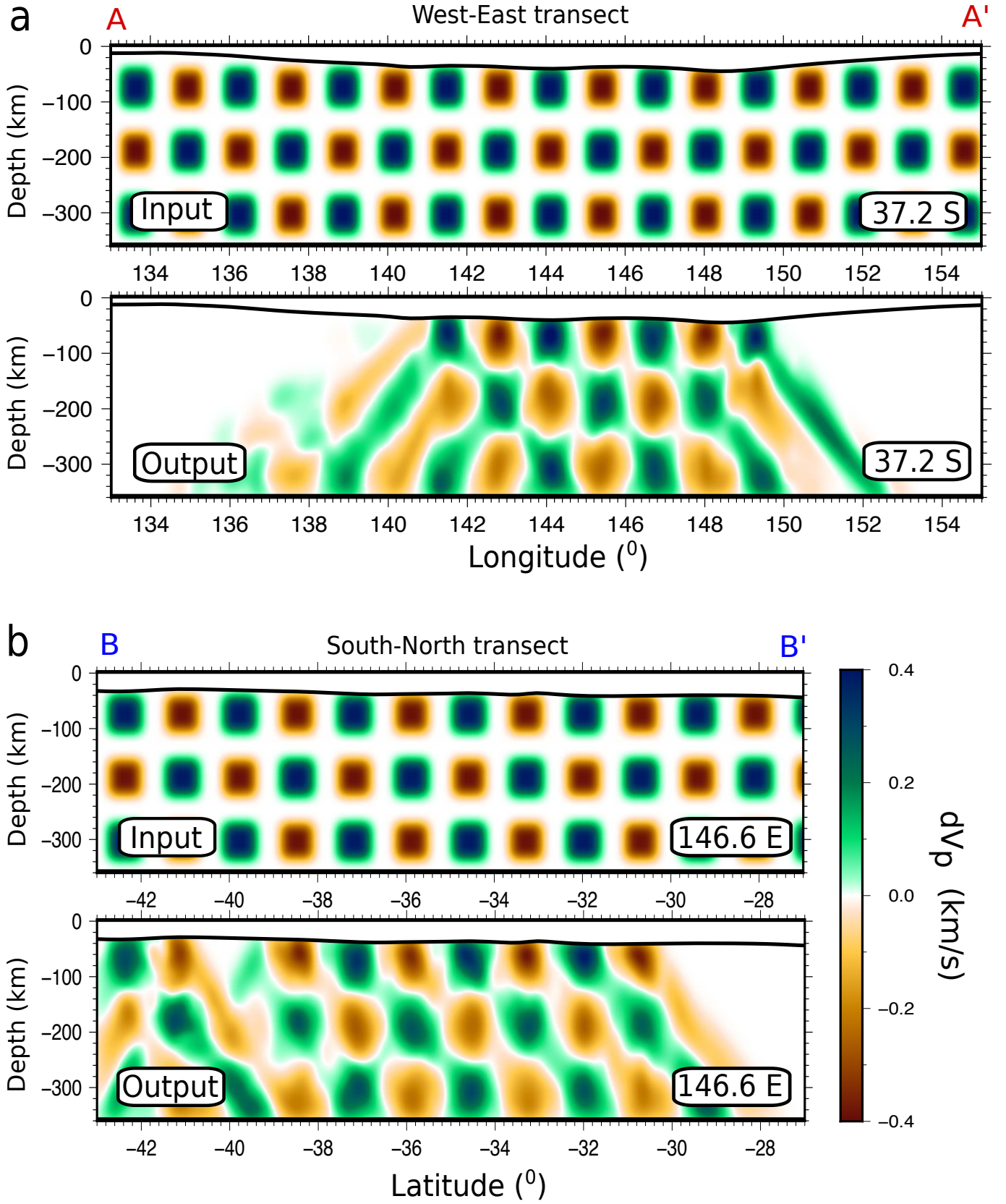


**Fig. 9:** Cross-sections illustrating the synthetic resolution test results. (A-A') Input and output test models at 37.2°S (see red line in Fig. 8a for location); (B-B') input and output test models at 146.6°E (see blue line in Fig. 8a for location).

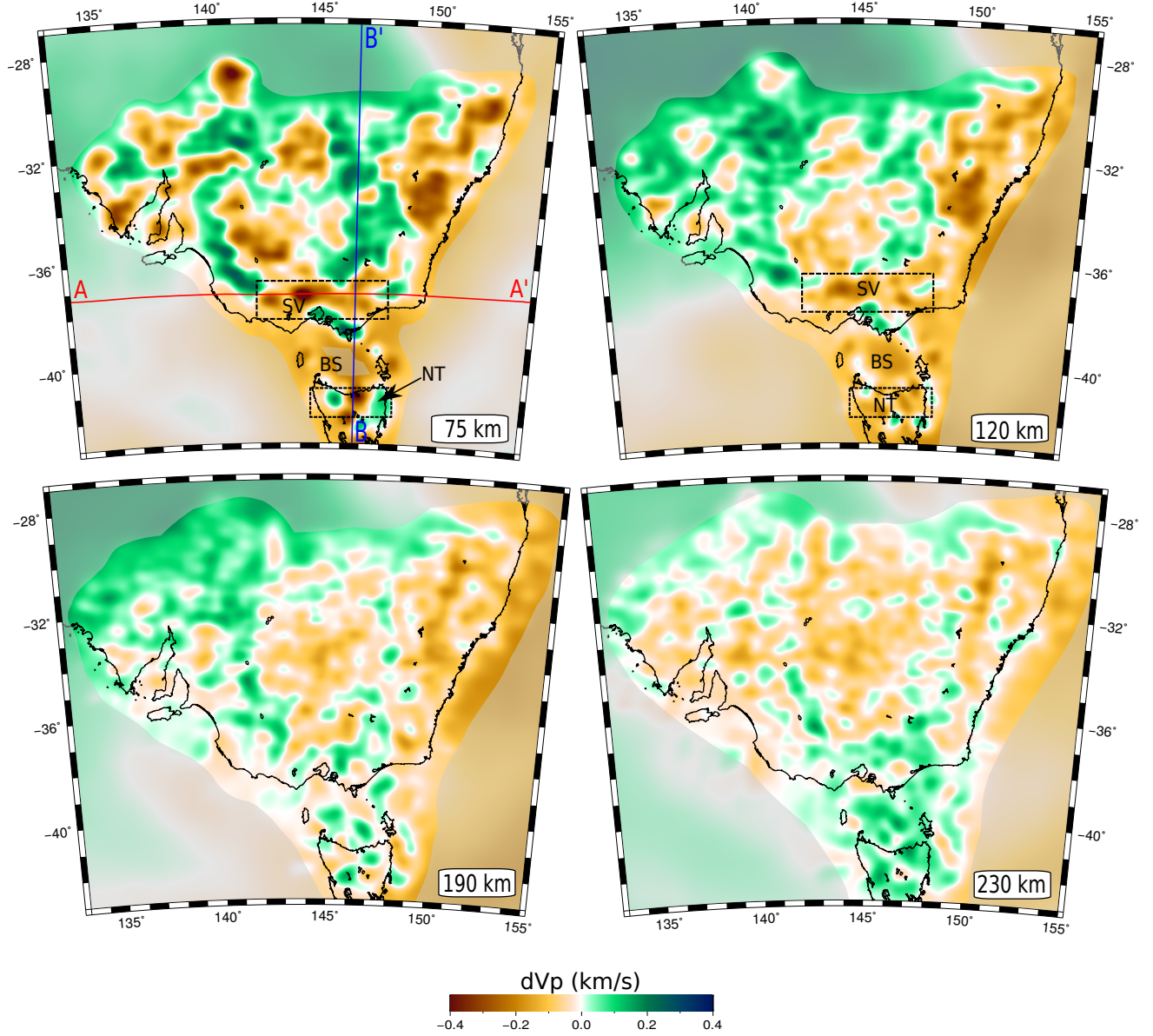


**Fig. 10:** Horizontal slices through the solution model obtained by inversion of relative arrival time residual data from the WOMBAT and BASS arrays. P-wave speed perturbations are relative to a 1-D depth-averaged version of the model. The gray mask denotes less resolved areas as determined by inspection of checkerboard test results for each depth slice. Several features are highlighted which are discussed in detail in the text: SV = Southern Victoria; NT = Northern Tasmania; BS = Bass Strait.



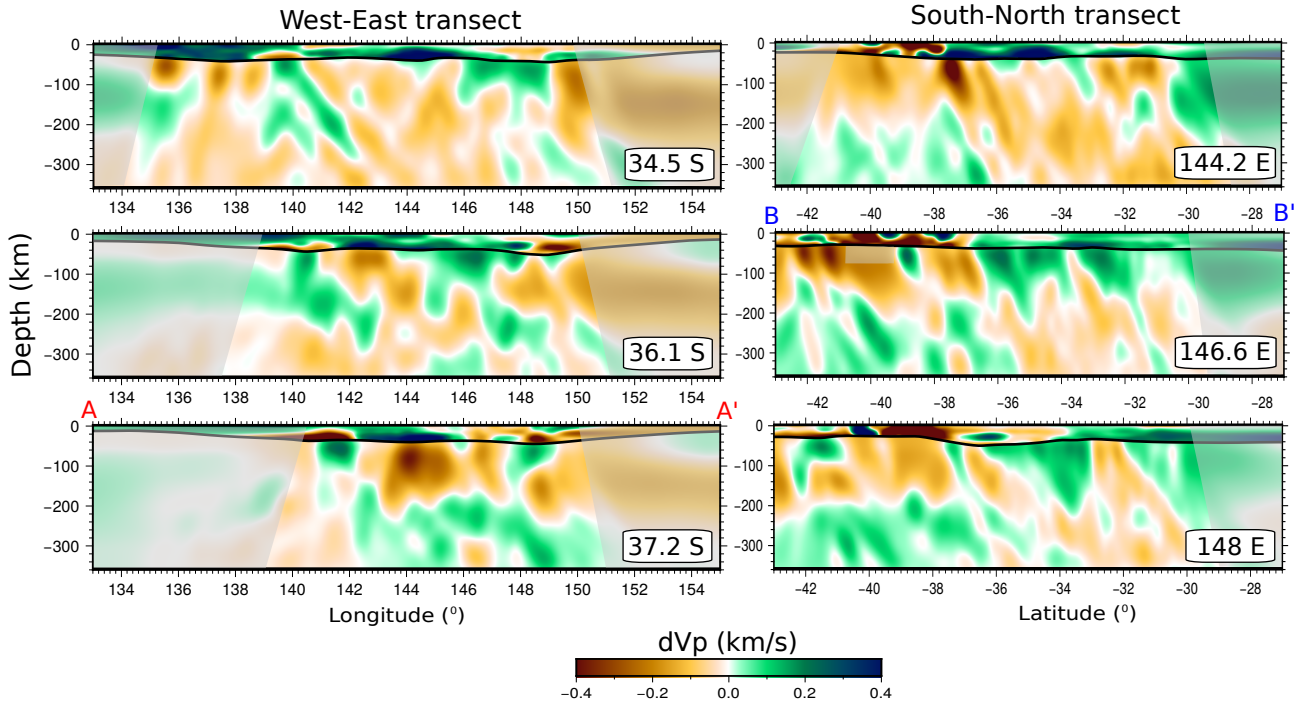


**Fig. 11:** Vertical slices through the solution model obtained by inversion of relative arrival time residual data from the WOMBAT and BASS arrays. As in Fig. 10, P-wave speed perturbations are relative to a 1-D depth-averaged version of the model. The gray mask denotes less resolved areas as determined by inspection of checkerboard results for each profile. See blue and red lines in Fig. 10 for locations of AA' and BB'.

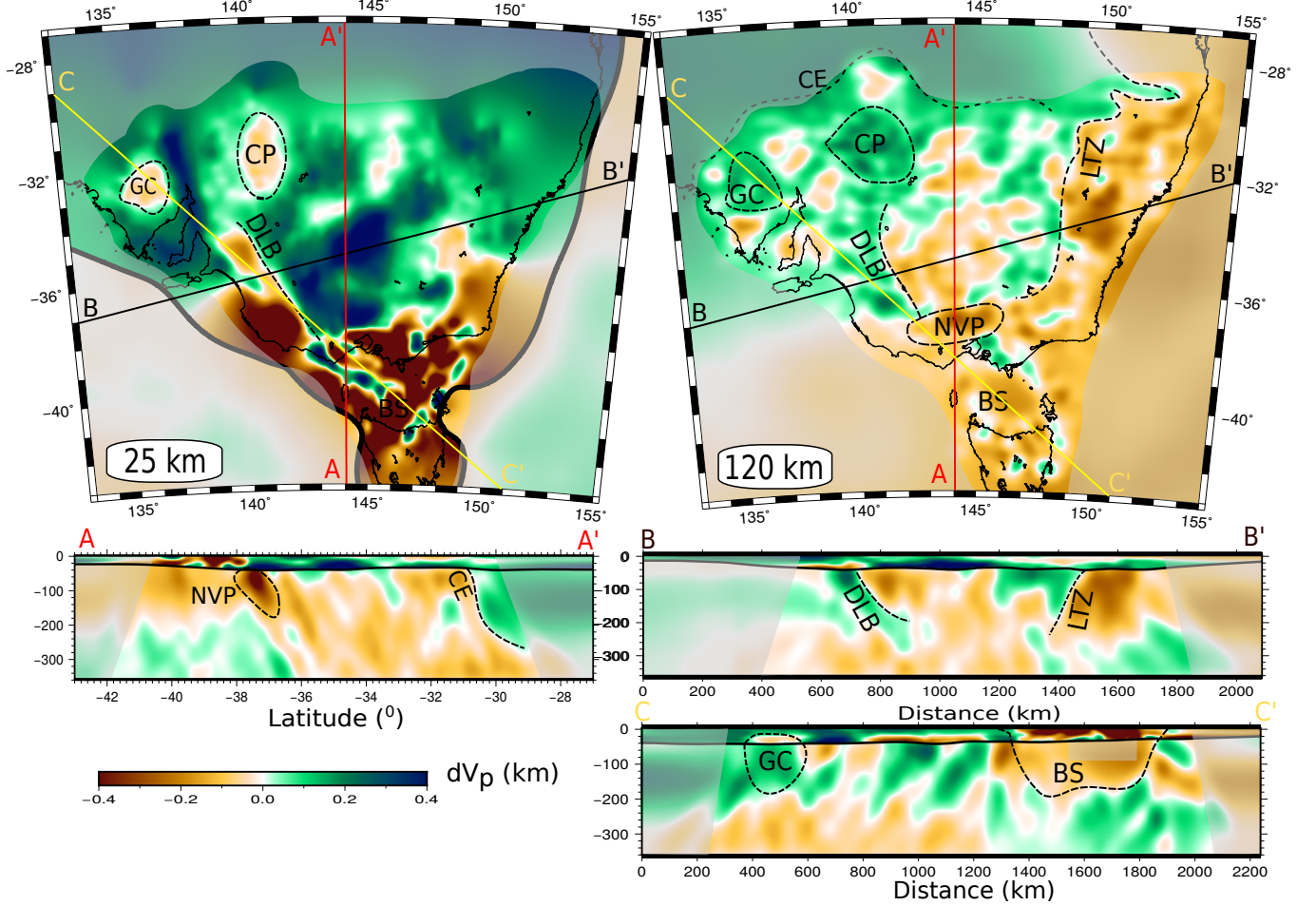


**Fig. 12:** Slices through the 3-D crust and upper mantle model of southeast Australia which uses the ambient noise crustal model and AuSREM Moho and upper mantle model in the starting model for the teleseismic data inversion. The locations of the three cross sections are denoted in both depth sections as coloured lines. Velocities are plotted relative to a reference one-dimensional model. The gray mask denotes less resolved areas as determined by inspection of checkerboard test recovery for each profile and depth slice. Several features are highlighted which are discussed in detail in the text: DLB = Delamerian-Lachlan boundary; LTZ = Lithosphere Transition Zone; NVP = Newer Volcanics Province; BS = Bass Strait; CE = Cron Edge; CP = Curnamona Province; GC = Gawler Craton. The velocity anomalies identified by the dashed lines are inferred to represent a signature at depth of what is observed at the surface.

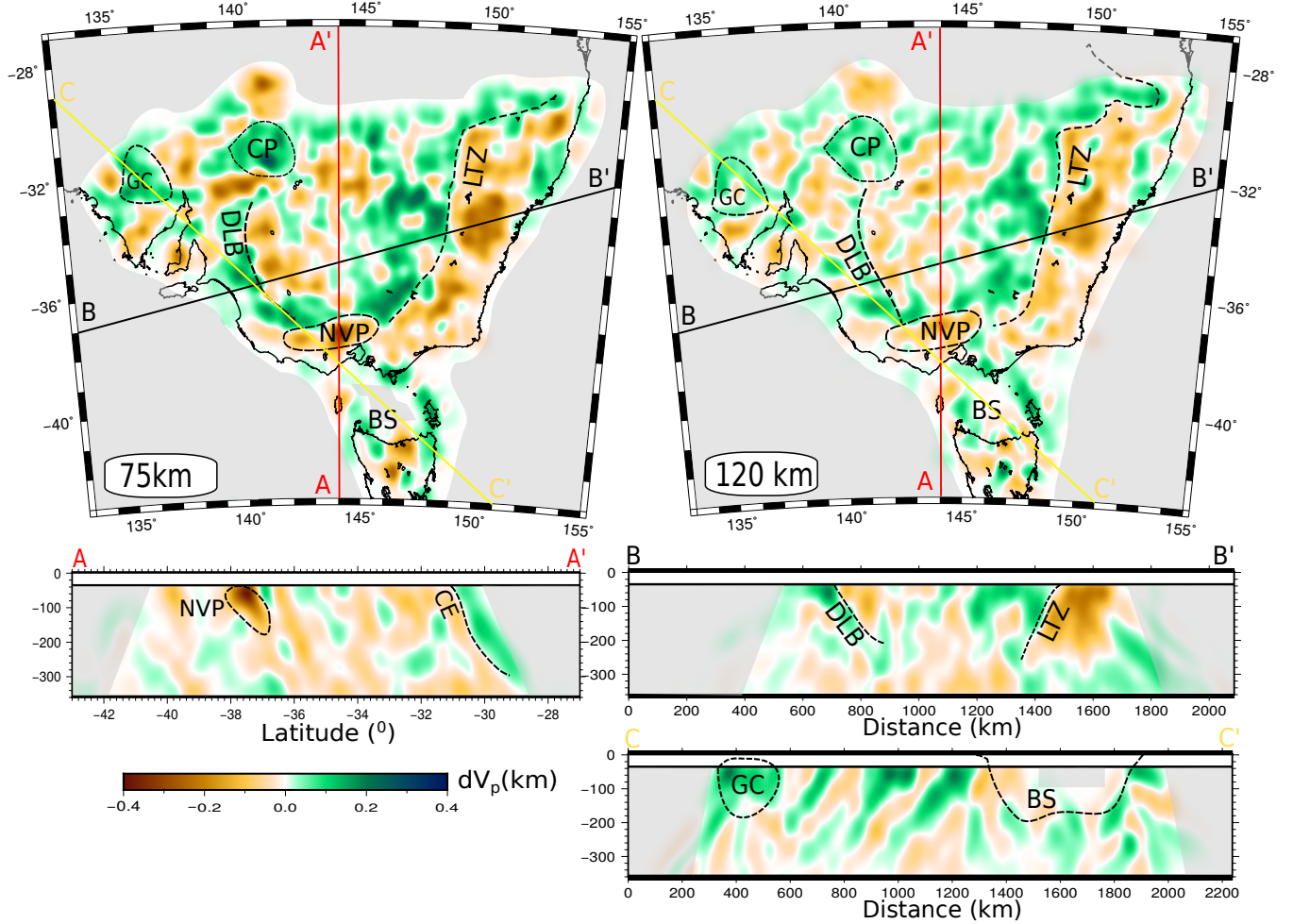


**Fig. 13:** Same as Figure 12 but now using a 1-D starting model (ak135) and a flat Moho for the teleseismic data inversion. The locations of the three cross sections are denoted in both depth sections as coloured lines. The gray mask denotes less resolved areas as determined by inspection of checkerboard test recovery for each profile and depth slice. Note the poor resolution in upper parts of the Bass Strait. Several features are highlighted which are discussed in detail in the text: DLB = Delamerian-Lachlan boundary; LTZ = Lithosphere Transition Zone; NVP = Newer Volcanics Province; BS = Bass Strait. CE = Cronon Edge; CP = Curnamona Province; GC = Gawler Craton. The velocity anomalies identified by the dashed lines are inferred to represent a signature at depth of what is observed at the surface.